Modeling Atmospheric Escape by the Discrete Velocity Method

Auteur : Dethier, William
Promoteur(s) : Munhoven, Guy; 8581
Faculté : Faculté des Sciences
Diplôme : Master en sciences spatiales, à finalité spécialisée
Année académique : 2018-2019
URI/URL : http://hdl.handle.net/2268.2/7837

Belgian Institute for Space Aeronomy - University of Liège

Department of Astrophysics, Geophysics and Oceanography

Modeling Atmospheric Escape by the Discrete Velocity Method

Thesis Submitted in Partial Fulfillment of the Requirements for the Degree of:

Master of Space Sciences

Author:
William Dethier

Advisors:
Dr. Justin Erwin
(BIRA - IASB)
Dr. Guy Munhoven
(ULiège)

Committee members:
Pr. Marc-Antoine Dupret
Dr. Benoît Hubert
Dr. Ann Carine Vandaele

Academic Year 2018 - 2019

Dedication

I dedicate the following work, which is the most societally recognised work I have achieved so far, to my mother, sister and father without whom this would have been much less attainable.

Acknowledgements

This thesis has been performed in the frame of an intership at the Belgian Institute for Space Aeronomy (BIRA - IASB) under an agreement with the university of Liège. I therefore wish to thank the university of Liège for giving me the opportunity and trusting me to go on this intership. Furthermore, I thank all the professors for giving me an invaluable source of education during my academic background.

I would like to thank Dr. Michael De Becker for his tremendous work of coordination for the master's students. He has been a great help to me when I needed advice on many topics.

I also wish to thank the Belgian Institute for Space Aeronomy for welcoming me as intern and for giving me access to their computer resources. I thank the whole staff for making this place a friendly environment. I want to thank Séverine Robert, Ian Thomas and Loïc Trompet for their good and lovely mood in the every day work in the office. Moreover, I want to thank Dr. Ann Carine Van Daele for allowing Dr. Justin Erwin to have me as intern to work on a more personal project. I also want to thank the Royal Belgian Observatory for renting me a room and making the stay easier.

I would like to thank Dr. Orenthal J. Tucker from NASA Goddard Space Flight Center for providing us with DSMC simulations to compare with the results obtained with DVM.

I thank any person who will read this work and hope they enjoy as well as the people who have taken the time to spell check it. I want to thank all the persons who gave me psychological support to complete this work.

I want to specially thank Dr. Guy Munhoven for supervising me during this project and also for his precious advice and discussions on various subjects.

Finally, I dearly thank Dr. Justin Erwin for his tutoring during this internship. I have learned so much in so short time. His expertise in planetary and computer science has helped me to accomplish this work in the most personally profitable way. I wish to be able to put into practise all that I have learned and go further in the scientific world.

Abstract

Atmospheric escape is an important process, which significant attention has been given to the last decades because it is necessary to understand characteristics of the different layers of an atmosphere, such as the thermosphere, the ionosphere or the exosphere.

Historically, studies of atmospheric escape were done using analytic models, for example Jeans theory or hydrodynamic escape. However, these techniques fail to correctly simulate the higher altitude layers where the particles' density is low and their velocity distribution begin to depart from a Maxwellian distribution so that the atmosphere can no longer be described as a fluid. More recently, kinetic modeling of escape have arisen and now simulations are commonly performed using the direct simulation Monte-Carlo (DSMC), which better describes the transition from collisional to collisionless regions of the atmosphere.

For the present work, we have considered a different kinetic technique, called the Discrete Velocity Method (DVM), that has not been as often used to address atmospheric escape problems. We have reproduced the DVM model of Merryfield and Shizgal (1994) and applied it to an idealised Earth-like neutral single component atmosphere. DVM is shown to be an effective technique and also time saving with respect to its statistical equivalent DSMC, when simulating atmospheric escape. In this manuscript, we first present a relevant scientific background on general atmospheric escape processes. Then, we explain the theory behind Boltzmann equation, the central equation to be solved. Finally we present a short section on numerical computation.

Then, we detail how we have built the complete model based on a step by step development where we go form a one-dimensional to a complete four-dimensional problem. Along this process, we investigate different combinations of finite difference schemes and features used to solve the Boltzmann equation and discuss why we decided to keep working with some particular combinations for the complete model.

Finally, we present the results from a series of simulations aimed at investigating a new lower boundary condition. Then, we compare them to fluid-Jeans and DSMC results. By doing so, we wish to qualify the technique and emphasize the consistency and relevance of DVM as well as the computation time saving it allows. The model we developed simulates a neutral hard sphere single component atmosphere. It is the basic form of the problem and it could be expanded by considering, for example, variable hard spheres, multiple components, external heating, photochemistry or taking into account ions and electrons.

Résumé

Durant les quelques dernières décennies, une certaine attention a été portée sur l'échappement atmosphérique. C'est en effet un procédé important car il permet de mieux comprendre les caractéristiques des différentes couches dans une atmosphère, telles que la thermosphère, l'ionosphère ou encore l'exosphère.

Historiquement, les simulations de l'échappement atmosphérique étaient réalisées à l'aide de modèles analytiques, comme la théorie de Jeans ou bien des modèles d'échappement hydrodynamique. Cependant, ces techniques ne simulent pas correctement les plus hautes couches atmosphériques là où les densités de particules sont basses et divergent d'une distribution maxwellienne, de telle sorte que l'atmosphère ne peut plus être décrite comme un fluide. Plus récemment, de nouvelles façons de faire ont été développées dans le cadre de l'échappement atmosphérique. Désormais, les simulations sont exécutées tout en utilisant une méthode kinétique appelée simulation directe de Monte-Carlo (DSMC). Cette technique permet de mieux décrire la transition entre les régions atmosphériques dominées par les collisions entre les particules et les régions où les collisions sont absentes.

Dans ce présent travail, nous avons considéré une technique kinétique appelée la méthode de vitesse discrète (DVM), qui n'a pas souvent été sollicitée en modélisation de problèmes liés à l'échappement atmosphérique. Nous avons reproduit le modèle de DVM de Merryfield and Shizgal (1994) et nous l'avons appliqué à une atmosphère terrestre neutre idéalisée et composée d'un type de particule. La DVM est démontrée efficace et apporte un gain de temps par rapport à la DSMC, son équivalent statistique, lorsqu'il est question de simulation d'échappement atmosphérique. Dans cet écrit, nous commençons par un rappel théorique concernant les concepts généraux des procédés d'échappement atmosphérique. Ensuite, nous expliquons la théorie utilisée dans l'équation de Boltzmann, qui est l'équation centrale du problème. Enfin, nous parlons brièvement d'un concept de calcul numérique utilisé.

Par la suite, nous détaillons la façon dont nous avons construit le modèle complet, basé sur un développement par étape où nous partons du problème à une seule dimension, pour arriver au problème complet à quatre dimensions. Au cours de ce procédé, nous avons investigué sur différentes combinaisons de schémas de différences finies ainsi que sur des astuces pour résoudre l'équation de Boltzmann. Nous y discutons également des diverses raisons de notre choix de continuer à travailler avec certaines combinaisons pour le modèle complet. Nous expliquons aussi comment nous avons résolu le problème en appliquant des schémas d'intégration spécifiques.

Finalement, nous présentons des résultats d'une série de simulations ayant pour but

d'investiguer sur l'utilisation d'une nouvelle condition de bord inférieure et ensuite nous comparons ceux-ci aux résultats de simulations fluid-Jeans et DSMC. En faisant ces comparaisons, nous voulons qualifier la technique de DVM et mettre l'accent sur sa pertinence ainsi que sur le gain de temps de calcul qu'elle permet d'atteindre. Le modèle développé simule une atmosphère neutre, composée d'un seul type de particules sphères dures. Il est la version de base du problème d'échappement atmosphérique et pourrait être étendu en considérant, par exemple, des particules sphères dures variables, une composition de plusieurs types de particules, un échauffement externe de l'atmosphère considérée, la photochimie ou bien en prenant en compte les ions et électrons.

Contents

Chapter 1

Introduction

When observing a planetary body in space, most of us probably wonder about the past of this body and also about its future. What did it look like one billion years ago and what will it look like in one billion years? Many factors must be taken into account when trying to answer these seemingly modest questions. Indeed, the evolution of a planetary body is very complex and requires many disciplines to join in order to be understood as fully as possible, as its influences range from its inner activity to its host star's activity, if it has any. Many scientific fields thus focus on describing each process individually and then assemble to make a continuously improving description of the universe's planetary bodies.
We, as many others, want to contribute to this goal by working on modeling the upper atmospheres. More precisely, we decided to work on atmospheric escape, which is the process by which an atmosphere is gradually loosing particles to outer space. This phenomenon can have a significant impact over a long duration of time. By modeling this process accurately we could better understand the time evolution of the atmosphere of a planet. For example, why has Mars apparently lost most of its water and why is its atmosphere so teneous? But it could also help predict how Earth's atmosphere is going to evolve and if it will ever look like Mars' or any other planet's.

Atmospheric escape was first mentioned in the late 19th century by John James Waterson and James C. Maxwell who were pioneers in the kinetic theory of gases as explained in Chamberlain (1963). Since then, atmospheric escape has been more intensively investigated and it is nowadays generally classified into two different types of escape. The first category is the *non-thermal escape* which contains subcategories such as *photochemical*, *ion* or *impact erosion* escape, but we will not describe this category further in this work[1].

The second one is the *thermal escape*. This category has two limiting cases: *evaporative escape* and *hydrodynamic escape*. The cases differ mainly because of the upper boundary they require as will be discussed later.
Hydrodynamic escape has been thoroughly described by Parker (1964). The theory

[1] *Remark:* Other effects can come into place when considering ionised particles and the process of escape can become different, although, we focused this work on neutral particles and shall not discuss non neutral effects even though they can be non negligible as particles can interact on long range without colliding.

was developed for the solar corona and explains that for particular conditions, an atmosphere can expand with a bulk velocity of the order of the speed of sound and thus most particles may eventually escape.
Evaporative escape has been pioneered by Jeans (1916) and later reworked by Chamberlain (1963). This atmospheric escape process states that above the exobase where the mean free path of particles is greater than the scale height, particles do not undergo collisions anymore. Some of the particles presenting a velocity greater than the escape velocity at the considered altitude are then assumed to escape and a flux or escape rate can be derived. Chamberlain (1963) considered that particles could enter different kinds of orbits related to their velocity after crossing the exobase boundary. Thus, particles can follow an orbit that will not reenter the planetary body's atmosphere. His work also adapted the definition of the number density that was used by Jeans (1916). This process is slower than the hydrodynamic process, although it can have a significant impact over a certain duration of time.

Investigation of the different macroscopic variables profiles of an atmosphere and its escaping rate most commonly call upon the steady-state Navier-Stokes fluid equations, where viscosity is neglected, considering a spherically symmetric atmosphere and a non-rotating frame of reference. Following Erwin et al. (2012), these equations include the conservation of mass equation

$$4\pi r^2 nu = \phi \tag{1.1}$$

where r is the radius, n is the number density, u is the bulk velocity, the equation of conservation of momentum

$$nm\frac{\partial}{\partial r}(\frac{1}{2}u^2) + \frac{\partial p}{\partial r} = -nmg(r) \tag{1.2}$$

where m is the mass of a particle, p is the pressure and g is the planetray body's gravitational acceleration and the equation of conservation of energy without heating

$$\frac{\partial}{\partial r}(\phi(C_p T + \frac{1}{2}mu^2 - U(r)) - 4\pi r^2 \kappa(T)\frac{\partial T}{\partial r}) = 0 \tag{1.3}$$

where C_p is the specific heat at constant pressure, T is the temperature, $U(r)$ is the gravitational energy and κ is the conductivity.

However, these fluid equations are only valid for lower layers of atmospheres where the velocity distribution of particles is sufficiently close to a Maxwellian. In higher layers, where collisions begin to be less frequent, they fail at accurately describing the atmosphere and therefore the escape rate. One way to get around this limitation that has been used over the past decades calls upon the non-linear Boltzmann equation which describes the fluid at the microscopic level. This equation contains a collision term and allows a more precise description of the regions where the transition between collision dominated regime to collisionless regime takes place. In other words, using the non-linear Boltzmann equation allows to study the atmospheric profile from below the exobase up to high exospheric altitudes. More details about the non-linear Boltzmann equation and its usage will be given in the following chapter.

The most commonly used technique to solve this problem is the Direct Simulation Monte Carlo (DSMC) . Unfortunately, DSMC suffers from statistical noise and becomes slow when it comes to simulating denser and lower parts of atmospheres. A potentially attractive alternative to overcome the short comings of DSMC is the Discrete Velocity Method (DVM). DVM is a numerical technique often used in rarefied gas dynamics to solve the Boltzmann equation (Broadwell, 1964; Cabannes, 1976; Gatignol, 1975). The technique discretises the velocity space and solves the underlying PDE using finite difference schemes. With this technique, the number of equations in the system to be solved can become quite large. However, the use of finite difference, allows to characterise the error in our solution on the basis of standard numerical error analysis, as opposed to DSMC which can be affected by statistical noise.
Our main objective was to reproduce the model presented in the paper "*Discrete velocity model for an escaping single-component atmosphere*" by Merryfield and Shizgal (1994) and eventually find possible improvements in order to have a more efficient model. Moreover, we contrasted these results with those obtained using DSMC and provided to us by Dr. Orenthal J. Tucker from NASA Goddard Space Flight Center, in order to show advantages of using discrete velocity method, such as computation time gain and numerical error reduction. Finally, we applied it to the atmosphere of an other planetary body to illustrate scientific relevance regarding planetary atmospheres in general.

Chapter 2

Scientific Backround

This chapter describes a few key theoretical concepts and specific notions used throughout this work.

2.1 Earth's Upper Atmosphere

Here we present common knowledge about the atmosphere to introduce the context of the work. We base the explanations on Figure 2.1 which displays the different classifications of the Earth's atmosphere depending on the considered characteristic. We focus our depiction on the upper parts of the atmosphere, that is above 100 km, as the model will simulate these regions.

2.1.1 Exosphere

This project uses the non-linear Boltzmann equation, which considers collisions between particles to describe atmospheric escape. The most important regions for us are those related to the collisional nature of the atmosphere, which is the barosphere and exosphere. The exosphere is the region where it is assumed that there are rare collisions between particles and that they approximately follow a free molecular flow or ballistic trajectories. It is separated from the barosphere, where collisions dominate, by the exobase. The exobase is an imaginary limit where the mean free path of a particle is equal to the local scale height. To determine the exobase location, generally, we look at the altitude where the Knudsen number is equal to 1. The Knudsen number is given by

$$K_n(r) = \frac{l(r)}{H(r)} \tag{2.1}$$

where $l(r)$ is the mean free path of the considered particles and is equal to

$$l(r) = \frac{1}{n(r)\sigma\sqrt{2}} \tag{2.2}$$

where σ is the particle's collisional cross section. $H(r)$ is the local scale height

$$H(r) = \frac{k_b T r^2}{GMm} \tag{2.3}$$

where G is the gravitational constant, M is the mass of the host body and k_b the Boltzmann constant.

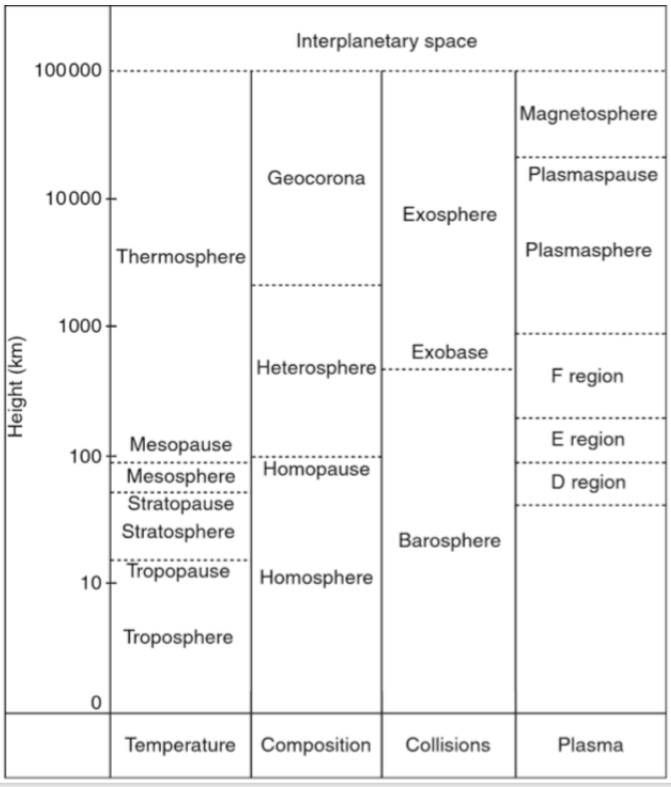

Figure 2.1: Different classifications of the vertical structure of the Earth's atmosphere (Grodent, 2019)

Actually, the transition between the two subregions is smooth and not strict. Below the exobase, at high altitude the velocity distribution function of the particles already deviates from a Maxwellian and far above the exobase collisions can still occur, although they become rarer. This smooth transition is due to the fact that the number density decreases with r. A good description of escape is one that follows and takes this gradual transition into account (Banks and Kockarts, 1973; Schunk and Nagy, 2000; Krasnopolsky, 2019) .

2.1.2 Thermosphere

The thermosphere is the upper subregion characterised by the evolution of the temperature in the atmosphere. In this region the temperature gradient is positive and higher in lower parts to become isothermal above. Temperatures typically range from $\sim$ 300 K to more than 1 000 K. The heating source in this region mainly comes from the EUV radiation absorption, such as by molecular oxygen. The heat sink comes from heat conduction to the region below called the mesopause. In the lower parts of the thermosphere a smaller amount of EUV photons arrives and temperature thus decreases. At higher altitudes, collisions become rare, hence temperature cannot be described macroscopically anymore. Some other conventions therefore use the exobase as the thermosphere's upper boundary, contrary to what is shown in Figure 2.1. (Banks and Kockarts, 1973; Schunk and Nagy, 2000; Krasnopolsky, 2019)

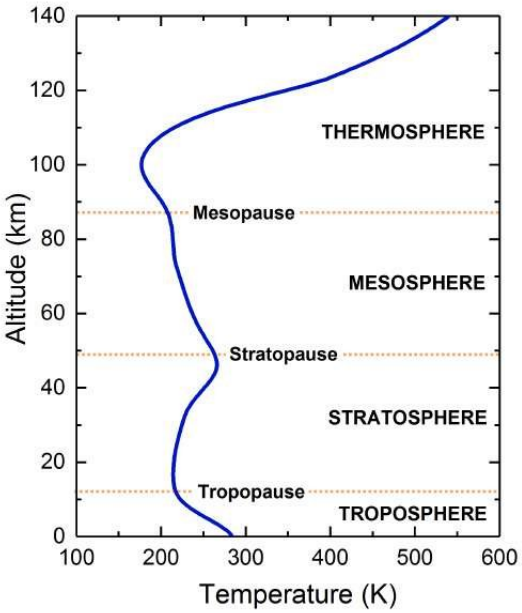

Figure 2.2: Thermal structure of the Earth's atmosphere. (Silber, 2018)

2.1.3 Heterosphere

The heterosphere is the region of the atmosphere characterised by non-homogeneity in its composition in contrast to the homosphere where eddy diffusion and molecular collisions mixe all the major components to have a uniform relative composition and allows the mean molecular mass to stay constant. As the density decreases higher in this region, the effects of turbulent mixing and molecular diffusion become inefficient and the particles are no more homogeneously redistributed. Above this, species tend to follow their individual scale heights, which depend on their masses. Because of this, lighter species such as hydrogen, helium and oxygen become enhanced and therefore the mean molecular mass decreases as can be seen in Figure 2.3 a. (Banks and Kockarts, 1973; Schunk and Nagy, 2000; Krasnopolsky, 2019)

2.1.4 Ionosphere

The ionosphere is the region characterised by the ionised nature of its components. It describes how ions and electrons are distributed in the atmosphere and it is influenced by the magnetic field of the Earth. The main albeit not unique source of formation of the ions is the photoionization of neutral particles by EUV and X-ray radiations, as well as cosmic rays. It spreads from about 60 km up to 1 000 km, it is present at all latitudes although it is sensitive to the Sun's activity and therefore, its exact composition and range vary on a day-night cycle. Above this region around the geomagnetic equator, is the plasmasphere which originates from the ionosphere and is a high ion density region located inside the closed magnetic field lines. These very complicated regions are influenced by many phenomenona that regulate their properties and the study of ionospheric processes is a whole individual field. Number density profiles of a series of ions are shown in Figure 2.3 b. (Banks and Kockarts, 1973; Schunk and Nagy, 2000; Krasnopolsky, 2019)

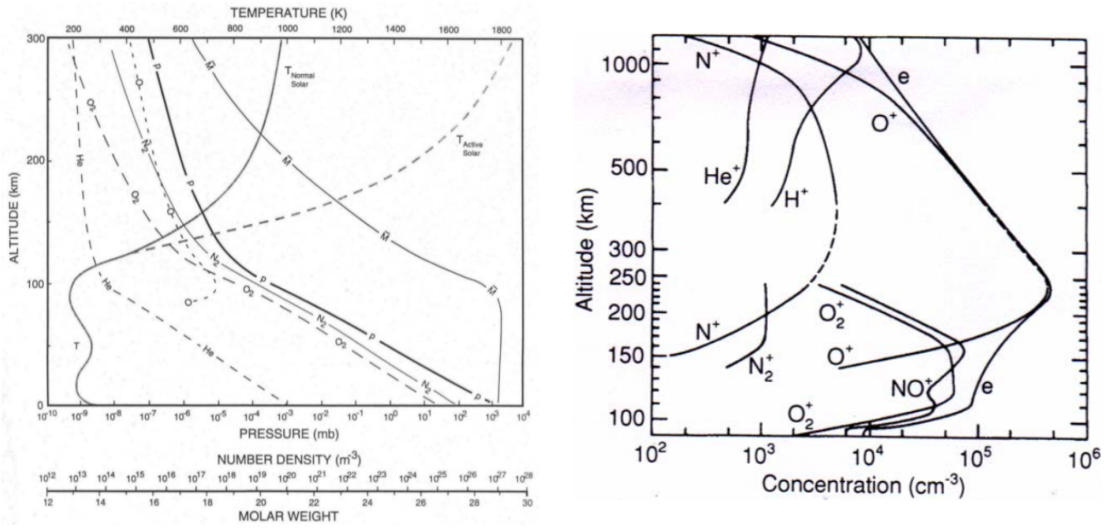

(a) (b)

Figure 2.3: (a) pressure, number density for different neutral component and mean molecular mass as function of altitude in Earth's atmosphere, (Grodent, 2019). (b) number density of positive ions and the electrons for a daytime ionosphere at solar minimum as function of altitude in Earth's atmosphere, (Banks and Kockarts, 1973).

Obviously all these regions have been defined from conventions and are in fact all existing together within the atmosphere of the Earth, meaning that they interact and influence each other. For example, the neutral particles often interact with charged particles, which eventually change the composition of their own regions. However, when trying to model one of these regions we are often restricted to make assumptions to simplify and neglect their interactions with one another, in order to have a reasonably fair model.

2.2 Thermal Escape

Here we detail the two limiting cases of thermal escape which are hydrodynamic escape and evaporative escape. Hydrodynamic escape is considered to be a fast escape rate, whereas evaporative escape is a slower, molecule by molecule escape process. The two regimes are shown in Figure 2.4 from (Volkov et al., 2011). Our description is mainly based on (Parker, 1964) for the former and on (Chamberlain, 1963) for the latter.

2.2.1 Hydrodynamic Escape

Parker (1964), with the goal to study the stellar coronal expansion, proposed to solve the system of equations formed by the hydrodynamic momentum equation and the equation of conservation of mass, using specific conditions.
First, he assumes a polynomial form for the temperature profile in the stellar corona as followed

$$T(r) = T_0 \left[\frac{N(r)}{N_0} \right]^{\alpha - 1} \tag{2.4}$$

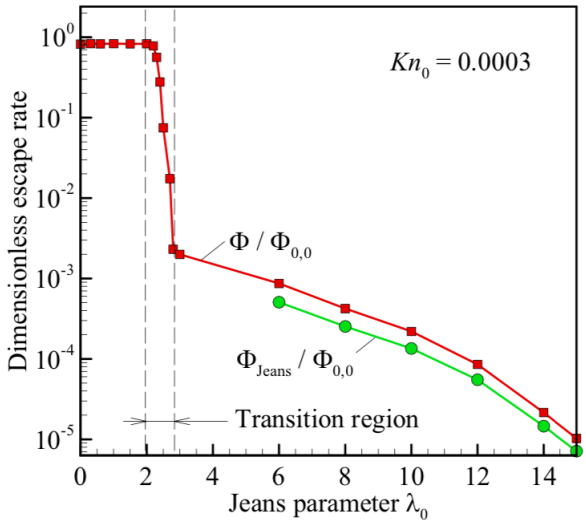

Figure 2.4: Representation of the limiting cases of thermal escape rate with respect to the Jeans parameter. Hydrodynamic escape rate is considered below $\lambda_0 = 2$ and evaporative escape rate (Jeans-like) above $\lambda_0 = 6$. These results were computed using DSCM model.

where $N(r)$ is the number density, T_0 is the temperature at the lower boundary of the corona and N_0 the number density at this boundary too, and is limited to the range of $\alpha \cong 1.1 - 1.2$.
He then argues the choice for the boundary conditions, which are that the expansion velocity at the lower boundary is small compared to the thermal velocity; the hydrostatic pressure tends to zero at infinity and the temperature decreases with increasing radial distance.
Together with these conditions, the non-linear system of equations yields solutions containing what is called a critical point. This point appears because of the competition between the thermal expansion term that decreases as $\frac{1}{r}$ and the gravitational term that decreases as $\frac{1}{r^2}$. Therefore, above a critical radius, the thermal expansion dominates, (Clette, 2018). This critical point can be seen when plotting the velocity with respect to the radius and different regions can be observed. In order for that point to exist, Parker has found that the temperature profile must decrease less rapidly than $\frac{a}{r}$, where a is the altitude at the base of the corona and that the gravitational field must be sufficiently intense. Therefore, this hydrodynamic expansion does not apply to every star or planetary body, but only in specific cases.
He also proved that the only solution for the corona to reach supersonic expansion is that its bulk velocity profile must cross the critical point, otherwise contradictions arise in solving the fluid equations and therefore subsonic velocity expansion solutions would not be allowed.
Finally, it is worth mentioning that hydrodynamic escape remains an approximation and that it fails at correctly describing the escape process at high altitude as the atmosphere cannot be considered as a fluid anymore because collisions become too rare (Catling and Kasting, 2017).

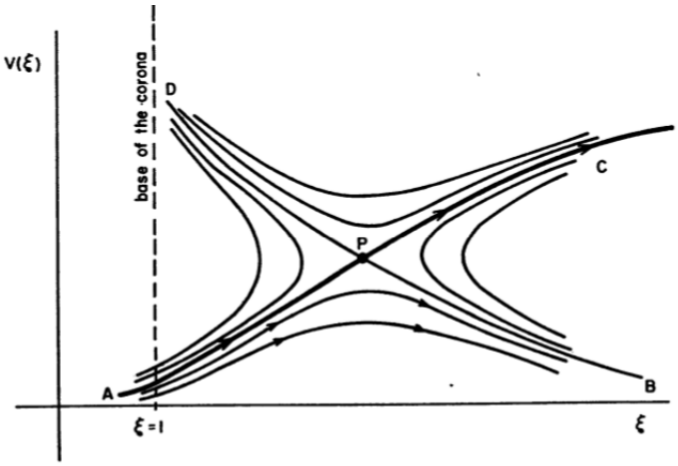

Figure 2.5: Plot of the the velocity with respect to the altitude scaled to the altitude of the base of the corona. It represents the solutions to the equations of conservation of mass and momentum from (Parker, 1964).

2.2.2 Evaporative Escape

The approximation of escape flux is given by the Jeans escape relationship which can be derived by integrating the Maxwell-Boltzmann distribution

$$f(\vec{v}) = \left(\frac{m}{2\pi T k_b}\right)^{\frac{3}{2}} \exp\left(-\frac{m\vec{v}.\vec{v}}{2Tk_b}\right) \tag{2.5}$$

over the velocity space. $\vec{v}$ represents the velocity of a particle in this equation. It basically describes how particles are distributed in the velocity space and how they are affected by temperature. At higher temperature particles can more easily reach greater velocities. The tails of the distribution contain the faster moving ones, the particles that can reach values greater than the escape velocity given by $v_{esc}(r) = \sqrt{\frac{2GM}{r}}$.
In order to get the flux, we need to integrate over the velocity space and multiply by the number density and the z component of velocity as follows

$$F = \int n v_z f(\vec{v}) dv^3 \tag{2.6}$$

In spherical coordinates the relation is

$$F_J = \int_0^{\frac{\pi}{2}} \int_0^{2\pi} \int_{v_{esc}}^{\infty} nv \cos\theta f(\vec{v}) v^2 \sin\theta \, dv \, d\phi \, d\theta \tag{2.7}$$

where we integrate from escape velocity to infinity for velocity, to get an escape flux. The result of these actions gives the flux in Equation 2.8 and the details are given in Appendix C.

$$F_J = n\sqrt{\frac{k_b T}{2m\pi}}(1+\lambda_e)\exp(-\lambda_e) \tag{2.8}$$

where λ_e is the Jeans parameter at the exobase and represents the competition between gravitational potential energy and thermal energy

$$\lambda = \frac{GMm}{k_b T r} \tag{2.9}$$

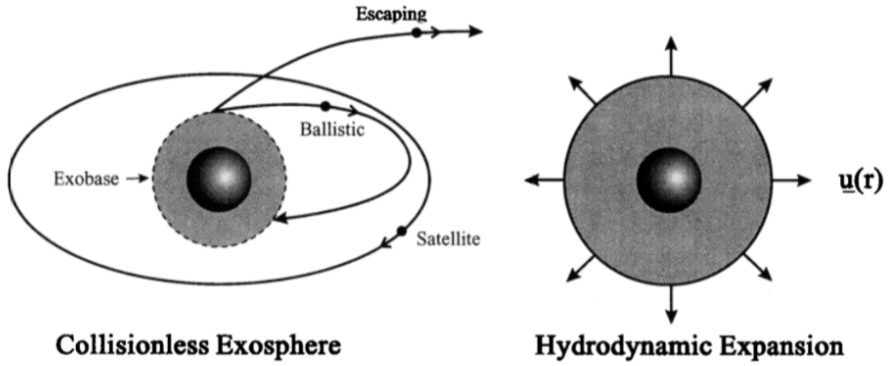

Figure 2.6: The two thermal mechanisms (Shizgal and Arkos, 1996).

This relation is an approximation saying that at an altitude where the mean free path of the particles is equal to the local scale height, a strict limit exists between collision dominated and collisionfree atmosphere. This limit is called the *exobase* and below, the standard fluid equations are applicable. Any particle crossing the exobase while bearing an upward velocity greater than the local escape velocity is assumed to escape from the atmosphere following open trajectories as it will not undergo collisions anymore.
Chamberlain (1963) studied three different trajectories for particles crossing the exobase. The first one is called the ballistic orbit, for which particles return. The second one is the satellite orbit, for which particles orbit the body, but do not enter back. The last one is the escaping orbit. He shows what the form of the partition function should be, depending on the different trajectories. This partition function multiplies the barometric density to solve a paradox of a finite density at $r \to \infty$ as well as an infinite mass for the atmosphere. His approach in deriving the escape relation is slightly different than the one we introduced.
Therefore, the knowledge of the number density and the temperature at a given altitude, would allow to compute the total escape rate of an atmosphere using Equation 2.8 and multiplying by the total spherical surface at this altitude

$$\Phi = F_J 4\pi r_e^2 \tag{2.10}$$

where r_e is the radius at the altitude of the exobase.
In a multi-component atmosphere the Jeans escape model tends to overestimate the escape as it considers an isothermal temperature (Pierrard, 2003). Indeed, if particles escape, then high velocity particles do not return to the atmosphere and thus energy is lost and temperature decreases. The Jeans escape flux is better suited in cases where $\lambda >> 1$, so that the escaping atmosphere only has a small impact on the lower layers of atmosphere. On the other hand, as shown by Merryfield and Shizgal (1994), Jeans escape can underestimate the escape rate in a single component atmosphere. Anyway, the outward moving flux of particles in an atmosphere can also be expressed as the product of the number density and the bulk velocity of the atmosphere. We can thus relate the Jeans escape flux to the outward moving flux by saying that the escape flux is the value of the outward moving flux at the exobase. This note brings us to the next point. As showed in (Erwin et al., 2012) we can couple the Jeans flux relation to the fluid equations addressed earlier in the introduction, to better estimate the escape flux. This method is known as the *fluid-Jeans model*.

2.2.3 Fluid-Jeans Model

We describe this method based on the paper by Erwin et al. (2012). The fluid-Jeans model considers an atmosphere in one dimension being the spatial radial dimension, it allows to obtain different radial profiles for variables such as the bulk velocity, the number density, the pressure and the temperature. The model uses the Jeans flux and the steady-state Navier-Stokes fluid equations, where viscosity is neglected, considering a spherically symmetric atmosphere and a non-rotating frame of reference.
One can start by using the following equation

$$\frac{\partial p(r)}{\partial r} = -nmg(r) \tag{2.11}$$

which considers the atmosphere to be hydrostatic and isothermal meaning that the temperature is constant throughout the atmosphere and that there is no general movement or no bulk velocity from particles. This relation considers that the gravitational attraction of the planet depends on the distance with r.
The integration of this equation yields

$$\begin{aligned}
\frac{dp(r)}{p(r)} &= -\frac{R^2}{r^2}\frac{mg_0}{k_bT}dr \\
\int_{p_0}^{p}\frac{dp(r)}{p(r)} &= \int_{R}^{r} -\frac{R^2}{r^2}\frac{mg_0}{k_bT}dr \\
\ln\frac{p(r)}{p_0} &= \left(\frac{1}{r}-\frac{1}{R}\right)R^2\frac{mg_0}{k_bT} \\
p(r) &= p_0\exp\left(\frac{R^2r}{r.r}\frac{mg_0}{k_bT} - R\frac{mg_0}{k_bT}\right) \\
p(r) &= p_0\exp\left(\frac{r}{H(r)} - \frac{R}{H(R)}\right)
\end{aligned} \tag{2.12}$$

where g_0 is the gravitational acceleration at R the radius of the considered body. The density is computed with the barometric law derived from the previous relation and given by

$$n(r) = n_0\exp(\frac{GMm}{k_bTr} - \frac{GMm}{k_bTR}) \tag{2.13}$$

where n_0 is the the number density at R. From the previous equation, the number density can be obtained if we know the temperature, which is initially assumed to be constant and also the number density at the surface. The pressure is derived in the same way using Equation 2.12 . Jeans's parameter is easily derived and by getting the value at the exobase we can derive Jeans escape flux using Equation 2.8. A more realistic model would require including the bulk velocity, i.e. the global motion of the atmosphere. This can be done by using the conservation of momentum equation

$$nm\frac{\partial}{\partial r}(\frac{1}{2}u^2) + \frac{\partial p}{\partial r} = -nmg(r) \tag{2.14}$$

where we only suppose that the atmosphere is isothermal. The as yet unknown bulk velocity can then be derived from the momentum equation written as in (Erwin

et al., 2012)

$$p(r) = p_0 \exp\left(- \int_{r_0}^{r} \frac{\frac{1}{2} m \frac{du^2}{dr} + mg(r)}{k_b T} dr \right) . \tag{2.15}$$

Using a simple numerical integration scheme we can solve the integral and obtain the radial pressure profile. The density profile can then be obtained by using the perfect gas law. Furthermore, we can compute the Jeans escape flux at the exobase. Once the flux is determined we use Equation 2.10 and equal it to the mass equation given by

$$4\pi r^2 n(r) u(r) = \phi(r) \tag{2.16}$$

which represents the molecular escape rate. Then we isolate the unknown u and obtain the bulk velocity profile from

$$\begin{aligned} F_J 4\pi r_e^2 &= 4\pi r^2 n(r) u(r) \\ u(r) &= \frac{r_e^2}{r^2} \frac{F_J}{n(r)} \end{aligned} \tag{2.17}$$

As the unknown in Equation 2.17 is used to solve Equation 2.15, we need to iterate between both several times to reach a steady result. Indeed our initial guess is a bulk velocity of 0. We thus use the computed value to recompute the results until the solution converges. Generally, five iterations are sufficient to reach convergence up to the eighth digit for our calculations.
Finally, even in the absence of external heating, the escape will cool the atmosphere and therefore the model will become non-isothermal. The equation used for this model is given by

$$4\pi r^2 n C_v \frac{\partial T}{\partial t} + \frac{\partial}{\partial r}(\phi(C_p T + \frac{1}{2} m u^2 - U(r)) - 4\pi r^2 \kappa(T) \frac{\partial T}{\partial r}) = 0 \tag{2.18}$$

where C_v is the specific heat at constant volume, C_p is the specific heat at constant pressure. U is the gravitational potential energy, κ is the conductivity.
This partial differential equation is solved numerically by using an implicit discretisation scheme to derive the value of the temperature after each iteration. After each time step we can recompute the solution of Equation 2.15 along with Equation 2.17 and Jeans escape, until reaching steady state for all the macroscopic variables.
In Figure 2.7 we show the radial profile of some macroscopic variables derived using the three model previously described. We can see that for the number density, the fluid-Jeans is the only model to significantly depart from the barometric solution and thus it is able to describe a more realistic number density. The fluid-Jeans also describes a decreasing temperature, which is expected as we consider escape and no heating. It also becomes constant at high altitudes due to the assumed conduction in the model, which transfers energy through collisions and tends to homogenise temperature. For the bulk velocity, the non-hydrostatic models show a non zero value at all altitudes, which is expected. As temperature stays higher for the isothermal case, the bulk velocity exhibits higher values than the complete fluid-Jeans model. For the outward molecular rates, the first model is zero which agrees with an hydrostatic model. The two other models show a non zero constant value which is consistent Equation 2.16. The greater value of isothermal case is a consequence of the higher value of bulk velocity.

We also show an other application where we derived the temperature profile using the fluid-Jeans for different initial temperatures. We find that too low a temperature makes that the atmosphere stays isothermal. On the other hand above a certain temperature, we find that the temperature decreases with r, which means that the initial temperature was high enough to trigger escape and that therefore the atmosphere looses energy and thus the temperature decreases. This exercise helps to know what minimum initial temperature to use if we want to simulate escape in a model and it justifies the temperature of 1 000 K chosen in (Merryfield and Shizgal, 1994) . However, the increase of temperature also expands the atmosphere and therefore, the exobase altitude moves upward. Increasing the temperature too much can move the exobase above the upper boundary of the problem. A way to check if the exobase is included in the model is to look at the altitude at which the Knudsen number equals one and compare it to the upper boundary value. In our simulation we were limited to around 1 200 K and we show the results in Figure 2.8.

The previous short description shows how this model is straightforward and allows to derive relevant results such as temperature and density profiles and an escape rate. However, as the model uses the fluid equations, it is not relevant to model high altitude atmosphere, where the collisions start to rarefy and where the distribution of velocity is no more a Maxwellian. What has been developed are other techniques that consider the evolution of the collisions throughout the atmosphere and model better the transition through the exobase. One of these techniques is called the discrete velocity method and is the one we use in this work.

2.3 Kinetic Methods

Using the Navier-Stokes equations is most valid when considering the atmosphere as fluid-like. It means that the density is high enough for the particles' velocity distribution to be considered Maxwellian. For these equations to be applied to the escape problem we must consider the atmosphere to be continuous up to the exobase as described above. However, number density decreases with altitude and the distribution of particles deviates from a Maxwellian making the use of these equations unjustified. Hopefully, other techniques can be applied, by solving the Boltzmann equation, to the entire atmosphere. This equation takes into account the simultaneous evolution of the distribution and the collisions. It can thus describe both continuum and rarefied flows.
As presented in Figure 2.9, we see how solving the Boltzmann equation is better suited for simulating high altitude atmosphere where even above the exobase collisions can still occur. In the past decades, the more common technique used to simulate the atmospheric escape in these different regimes has been the DSMC method, thoroughly explained in (Bird, 1994). This statistical method has been used because it is well suited for simulating rarefied gas dynamics. DSMC allows deriving properties of the atmosphere similar to the fluid-Jeans method, but by considering the atmosphere at the molecular level and not as a continuum. It uses the probability of the post-collision redistribution of particles' velocities to simulate the evolution of the layers of the atmosphere using values as the number density, the relative velocity between particles along with their probabilistic cross section etc. However, DSMC becomes slow when simulating denser regions of the atmosphere

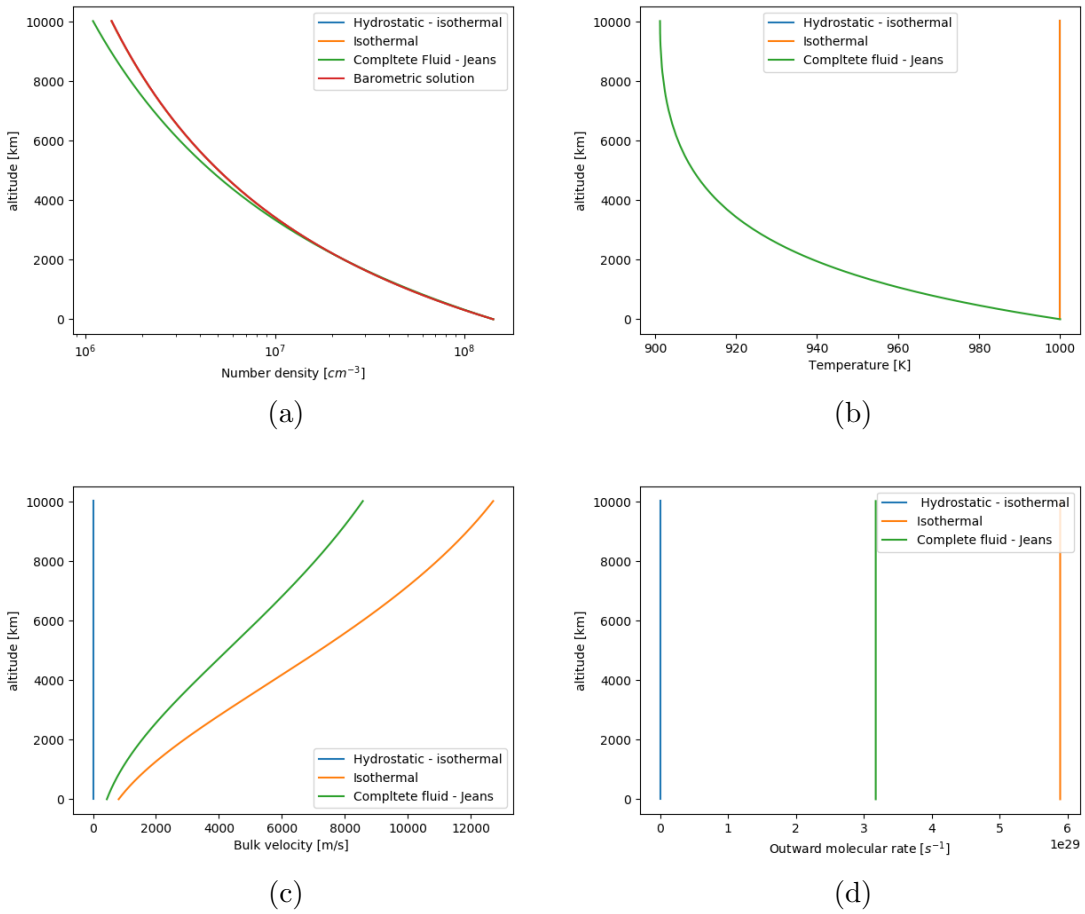

Figure 2.7: Plots of the macroscopic variables derived from the fluid-Jeans model for an initial temperature of 1 000 K, a surface number density of $1.417 \times 10^8 \mathrm{cm}^{-3}$ and the parameters corresponding to an Earth-like planet with an hydrogen atmosphere. The upper boundary was set at 16 400 km and we iterated until steady state with a time step of one day for the complete fluid-Jeans part.

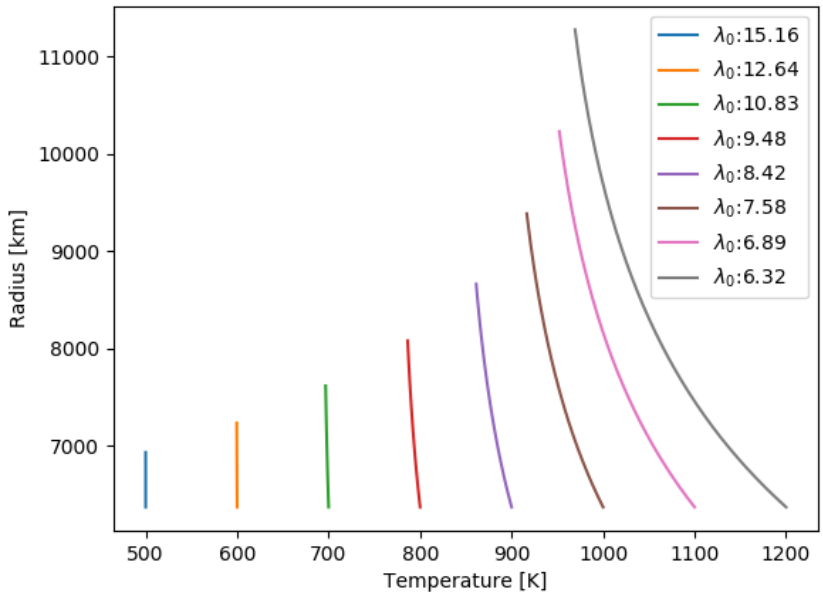

Figure 2.8: Temperature profile cut at the exobase altitude for different initial temperatures derived using the complete fluid-Jeans model.

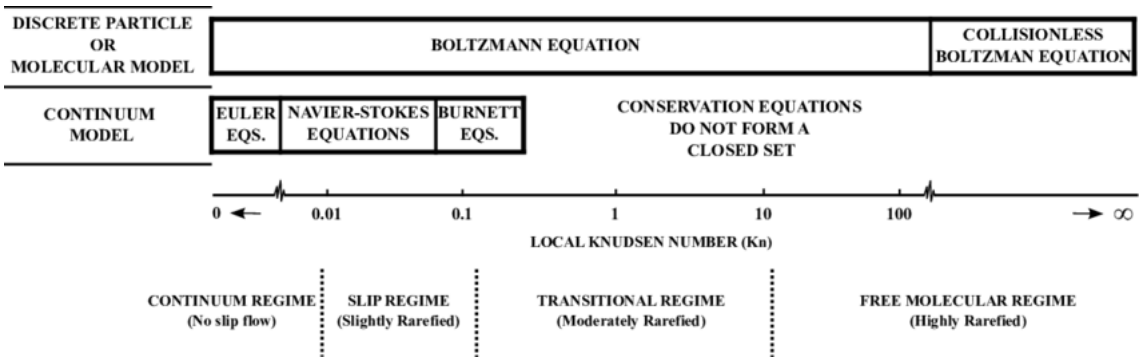

Figure 2.9: Different mathematical descriptions of fluids and their domain of application with respect to the Knudsen number. From Palharini (2014).

because it becomes computationally expensive. Furthermore, as it is a statistical method it uses a large number of particles, which inevitably introduces statistical noise into the calculations, (Bird, 1994).

An alternative technique to solve the Boltzmann equation is the Discrete Velocity Method (DVM). It is a numerical technique often used in rarefied gas dynamics. To our best knowledge, it has only rarely been used to simulate dynamics of the atmosphere, for example Merryfield and Shizgal (1994) have applied DVM to the planetary escape problem, but mostly in particular rarefied flows related situations, for example (Gatignol, 1975; Cabannes, 1976; Broadwell, 1964). As already explained earlier, the main aspect of this technique is to discretise the velocity space and solve a partial differential equation using finite difference schemes.

2.4 Non-Linear Boltzmann's Equation

Here we explain a bit more the foundations of the non-linear Boltzmann's equation, following the development by (Schunk and Nagy, 2000).
This equation deals with the particles' velocity distribution function. This distribution is characterised by three independent variables: the position in space, the position in the velocity space and time. The two first variables form what we call the phase space. The distribution describes the amount of one type of particles that can be found in a specific volume element around the position in space and that have a specific range of velocities in a velocity space element around the velocity position at a specific time. With the non-linear Boltzmann equation we look at the time evolution of the distribution in this phase space under collisions and external forces. The collisions will act in the *production* or *loss* of particles in the distribution. Indeed, after a collision, a particle can change velocity and therefore change the number of particles possessing a certain velocity and thus the distribution. After a collision a particle can also leave the space element and therefore deplete the distribution. The evolution with time of the velocity distribution of particles 1, called f_1 is given by

$$\frac{df_1}{dt} = \lim_{\Delta t \to 0} \frac{f_1(\vec{r} + \Delta\vec{r}, \vec{v}_1 + \Delta\vec{v}_1, t + \Delta t) - f_1(\vec{r}, \vec{v}_1, t)}{\Delta t} \tag{2.19}$$

where $\vec{r}$ is the position in space and $\vec{v}_1$ is the position in velocity space.
When considering the limit, the first term of the numerator can be expanded and we have

$$\frac{df_1}{dt} = \lim_{\Delta t \to 0} \frac{1}{\Delta t} \left[f_1(\vec{r}, \vec{v}_1, t) + \frac{\partial f_1}{\partial t}\Delta t + \Delta\vec{r} \cdot \nabla f_1 + \Delta\vec{v}_1 \cdot \nabla_v f_1 + ... - f_1(\vec{r}, \vec{v}_1, t) \right] \tag{2.20}$$

When taking the limit we have

$$\frac{df_1}{dt} = \frac{\partial f_1}{\partial t} + \vec{v}_1 \cdot \nabla f_1 + \vec{a}_1 \cdot \nabla_v f_1. \tag{2.21}$$

The right-hand side of the above equation represents the left-hand side of the non-linear Boltzmann equation. If collisions are not taken into account, then the latter becomes zero and we have $\frac{df_1}{dt} = 0$, the equation is now called Vlasov equation.
On the other hand, if we consider collisions then the right-hand side of the non-linear

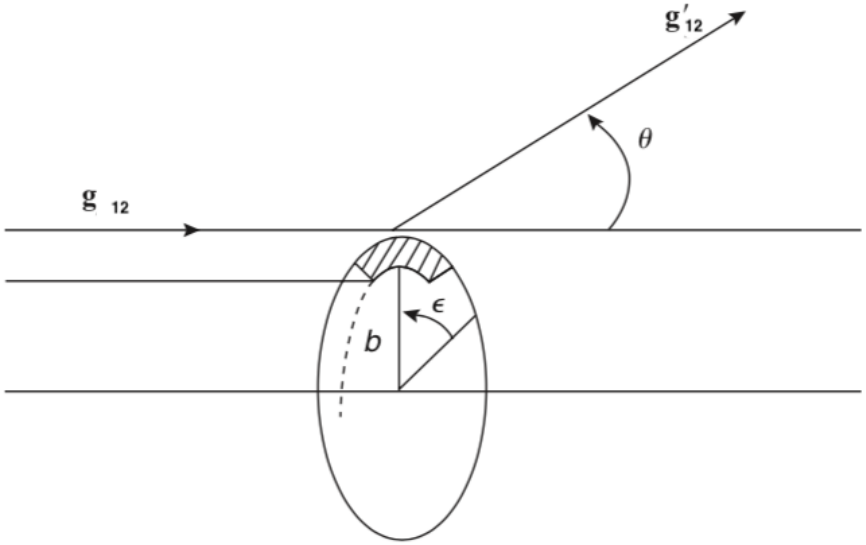

Figure 2.10: The relative velocities before and after the collision are g_{12} and g'_{12}, respectively, b is the impact parameter, ϵ is the azimuthal angle that defines the plane of the collision, and θ is the scattering angle. The cross-hatched area is $bdbd\epsilon$. Taken from (Schunk and Nagy, 2000).

Boltzmann equation is non-zero and it is called the collision integral. Therefore, we have

$$\frac{df_1}{dt} \equiv \frac{\delta f_1}{\delta t} = \frac{\delta f_1^+}{\delta t} - \frac{\delta f_1^-}{\delta t} \tag{2.22}$$

where $\frac{\delta f_1}{\delta t}$ represents the change of the distribution due to collisions and where the first term of the right-hand side is the *production* or change of the distribution due to particles acquiring a velocity in the velocity space element defined earlier. The second term of the right hand side is the *loss* or change of the distribution due to particles acquiring a velocity outside the velocity space element defined earlier. We describe the collision between different types of particles by starting with the *loss* term as it was done in the reference book (Schunk and Nagy, 2000). For collisions to happen the particles have to be in the same spatial volume element dr^3 as we consider only binary elastic collisions between neutral particles. Therefore, particles 1 will face a flux formed by particles 2 having a velocity volume element dv_2^3. In the interval of time dt this flux covers a spatial volume of

$$g_{12}.dt.b\,db.d\epsilon \tag{2.23}$$

where g_{12} is the relative velocity between the two types of particles before the collision, b is the impact parameter and ϵ the collision plane from Figure 2.10. The number of collisions that occur in this volume in the time dt between the flux of particles 2 and the number of particles 1 is:

$$f_1.dv_1^3\,dr^3.f_2.dv_2^3.g_{12}.dt.b\,db.d\epsilon \tag{2.24}$$

It corresponds to the number of particles 1 that will be scattered out of the velocity volume element dv_1^3 . Now, to get the total number of scattered particles 1, we

need to consider all velocities of particles 2, all impact parameters and all angles of collision. We derive it by integrating as follows

$$f_1.dv_1^3 dr^3.dt \int\int\int f_2.g_{12}.b\, dv_2^3\, db\, d\epsilon \tag{2.25}$$

We retrieve $\frac{\delta f_1^-}{\delta t}$ by dividing the relation by $dv_1^3\, dr^3\, dt$

$$\frac{\delta f_1^-}{\delta t} = \int\int\int f_1 f_2.g_{12}.b\, dv_2^3\, db.d\epsilon \tag{2.26}$$

Now we describe the *production* term $\frac{\delta f_1^+}{\delta t}$, which represents particles 1 inside the volume element dr^3 and outside the velocity element dv_1^3 that acquire a velocity belonging in the velocity element dv_1^3 after a collision with particles 2 from a velocity element $dv_2^{3'}$ .Schunk and Nagy (2000) call this an inverse collision. As we consider binary elastic collisions we are allowed to say that the inverse collision is symmetric with respect to the initial collision. This means that a particle 2 is in the same impact parameter range and the same collision plane range as in the first case for the loss term. Therefore, particles 1 in $dv_1^{3'}$ will face a flux formed by particles 2 having a velocity volume element $dv_2^{3'}$. During a time interval dt this flux covers a spatial volume

$$g_{12}^{'}.dt.b\, db.d\epsilon \tag{2.27}$$

The number of collisions that occur during dt between the flux of particles 2 in this volume and the number of particles 1 is:

$$f_1^{'}.dv_1^{3'}\, dr^3.f_2^{'}.dv_2^{3'}.g_{12}^{'}.dt.b\, db.d\epsilon \tag{2.28}$$

It corresponds to the number of particles 1 scattered into the velocity volume element dv_1^3 . Now, to get the total number we need to consider all the velocities of particles 2, all the impact parameters and all angles of collision. We derive it by integrating as follow:

$$f_1^{'}.dv_1^{3'}\, dr^3.dt \int\int\int f_2^{'}.g_{12}^{'}.b\, dv_2^{3'}\, db.d\epsilon \tag{2.29}$$

A few considerations have to be mentioned. In a binary elastic collision the relative velocity between two types of particles are equal for the cases of inverse collision and its counterpart. Then, to link both velocity volume elements, we use the Jacobian of the change of variables,[1] $|J| = \frac{\partial(\vec{v}_1^{'},\vec{v}_2^{'})}{\partial(\vec{v}_1,\vec{v}_2)} = 1$, as follows

$$dv_1^{3'} dv_2^{3'} = dv_1^3 dv_2^3 |J| \tag{2.30}$$

By applying it to Equation 2.29 we obtain

$$f_1^{'}.dv_1^3 dr^3.dt \int\int\int f_2^{'}.g_{12}.b dv_2^3 db.d\epsilon \tag{2.31}$$

We retrieve $\frac{\delta f_1^+}{\delta t}$ by dividing the previous relation by $dv_1^3\, dr^3.dt$

$$\frac{\delta f_1^+}{\delta t} = \int\int\int f_1^{'} f_2^{'}.g_{12}.b dv_2^3 db.d\epsilon \tag{2.32}$$

[1] Please see theory on binary elastic collision to know how to derive the value of the Jacobian, e.g. (Schunk and Nagy, 2000)

Then, Equation 2.22 becomes

$$\frac{\delta f_1}{\delta t} = \int\int\int (f_1^{'} f_2{}' - f_1 f_2).g_{12}.b dv_2^3 db.d\epsilon \tag{2.33}$$

The form used in (Merryfield and Shizgal, 1994) is derived by linking a differential cross section to the impact parameter and collision plane as

$$\begin{aligned} db\, d\epsilon\, b =& \sigma_{12}(g_{12}, \theta) \sin\theta d\theta d\epsilon \\ =& \sigma_{12}(g_{12}, \theta) d\Omega \end{aligned} \tag{2.34}$$

where Ω is the solid angle in the colliding particles center of mass reference frame, θ is the scattering angle of the center of mass, σ is the differential scattering cross section. The complete non-linear Boltzmann equation is given by

$$\frac{\partial f_1}{\partial t} + \vec{v}_1 \cdot \nabla f_1 + \vec{a}_1 \cdot \nabla_v f_1 = \int\int (f_1^{'} f_2{}' - f_1 f_2).g_{12} \sigma_{12}(g_{12}, \theta) dv_2^3 d\Omega \tag{2.35}$$

2.5 Solving a PDE; the CFL Condition

In numerical analysis, when using finite differences for solving differential equations, care has to be given to the lengths of the integration steps chosen. Indeed, choosing too large a value can induce instability to the solution. Let us take the example of hyperbolic partial differential equations and the case of the advection equation, which is relevant to our problem as they share the first two terms

$$\frac{\partial f(t,r)}{\partial t} + a\frac{\partial f(t,r)}{\partial r} = 0 \tag{2.36}$$

where a is a positive constant and may be associated to the vertical velocity component of our problem, t is a temporal coordinate and r a spatial coordinate, (Morton and Mayers, 2005). Now by developing the equation with finite difference using a first-order upwind scheme for the spatial derivative and a first order forward difference scheme for the time derivative we get

$$\frac{f(t+1,r) - f(t,r)}{\Delta t} + a\frac{f(t,r) - f(t,r-1)}{\Delta r} = 0 \tag{2.37}$$

for positive values of a and

$$\frac{f(t+1,r) - f(t,r)}{\Delta t} + a\frac{f(t,r+1) - f(t,r)}{\Delta r} = 0 \tag{2.38}$$

for negative values of a, meaning particles going downward in our model. The values of Δt and Δr must not be randomly chosen. They must comply to a condition called the Courant–Friedrichs–Lewy or CFL condition to yield a stable solution over time when using an explicit scheme for solving hyperbolic partial differential equations. The condition is written as such

$$C = a\frac{\Delta t}{\Delta r} \tag{2.39}$$

with C the Courant number. This number generally takes a value that depends on the whole partial differential equation. For the first-order upwind scheme, described

above, it must be less or equal to 1 for stability (Hirsch, 2007) and the condition becomes

$$\Delta t \leq \frac{\Delta r}{a} \tag{2.40}$$

The condition can be understood as followed. If we take the highest value of velocity for a and the lowest value of Δr we get the maximum value of Δt. This means that particles with the highest velocities must not in an interval Δt travel a greater distance than Δr, otherwise they would fall outside the stencil of the finite difference in r and we would get a wrong solution for this time step, which will reverberate in the next time step solution and so on. We then see the importance to respect the condition if we want to obtain a stable solution over time, see also (Arnst, 2018; Isaacson and B. Keller, 1994). Although, in our model, the upwind scheme was of second order, variable coefficients were present and the right-hand side was non-linear. This means we had to try several different combinations of Δt with Δr based on the case introduced above because the derivation of the exact CFL condition for our model is beyond the scope of our work.
For example, if we take the value of $v_{max} = a = 12\text{km.s}^{-1}$ and our smallest r grid space which is 211.8km for twenty spatial points and 101.5km for fourty spatial points, we have that $\Delta t \leq 17.6$s and $\Delta t \leq 8.44$ s respectively. We thus made the simulations using a time step of 10s and 5s to be safe. However, we had to go to 2.5 s for the fourty spatial points to avoid numerical oscillations. This shows that the CFL condition is a rough upper limit for stability. For the velocity derivatives of the Boltzmann equation, we also used this condition, but the condition on the spatial derivative was, in all the simulations, stronger. We therefore relied on the values given by the condition on the spatial derivative for the different simulations done.

Chapter 3

Description of the Problem

In this chapter, we describe our modus operandi for solving the central question of this work, alongside with an explanation on the different pieces that compose this question. Eventually, we present a series of representative results that, in our opinion, are most relevant for comprehension and visualisation.
The model of Merryfield and Shizgal (1994) aims at simulating atmospheric escape from a planetary body and does so by solving the non-linear Boltzmann equation

$$\frac{\partial f}{\partial t} + (\vec{c} \cdot \nabla_r) f + (\vec{a} \cdot \nabla_c) f = \int \int [f_1' f_2' - f_1 f_2] \sigma(g, \Omega) g \, d\Omega \, dc_2 \tag{3.1}$$

using the discrete velocity method.

To use discrete velocity method on the non-linear Boltzmann equation, we used the form for spherically symmetric atmosphere with Cateisan velocity derived in (Merryfield and Shizgal, 1994) and given as

$$\frac{\partial f}{\partial t} + v_z \frac{\partial f}{\partial r} - \frac{1}{r} \left[v_x v_z \frac{\partial f}{\partial v_x} + v_y v_z \frac{\partial f}{\partial v_y} - (v_x^2 + v_y^2) \frac{\partial f}{\partial v_z} \right] - \frac{GM}{r^2} \frac{\partial f}{\partial v_z} = C[f] \tag{3.2}$$

where we used finite difference schemes on the derivatives to work with the discretised form. $C[f]$ is the non-linear Boltzmann collision integral expressed in Cartesian velocity components and is given by

$$C[f] = \sum_{j=1}^{p} \sum_{k,l} A_{ij}^{kl} (f_k f_l - f f_j) \cdot \Delta v^3 \tag{3.3}$$

with A_{ij}^{kl} coefficient being equal to

$$A_{ij}^{kl} = \sigma_0 |v_i - v_j| / C_{ij} \tag{3.4}$$

with C_{ij} being the number of outcomes from the collision between particles i and j and σ_0 the total momentum collisional cross section of a particle given as

$$\sigma_0 = \pi d^2 \tag{3.5}$$

where d is the collisional diameter of the considered particles.
The description on how to go from Equation 3.1 to Equation 3.2 is given in Appendix B. For the Discrete Velocity method a discrete velocity space is adopted in which we

consider that particles can have a certain finite number of different velocity vectors. Generally, we choose a discrete velocity space with ten to twenty values. The range is chosen such that the escape velocity

$$v_{esc}(r) = \sqrt{\frac{2GM}{r}} \tag{3.6}$$

is encompassed and that the standard deviation of the Maxwell distribution

$$v_t = \sqrt{\frac{k_b T_0}{m}} \tag{3.7}$$

is greater than the velocity space resolution and is at least covered three times, where T_0 is the initial temperature of the atmosphere. This ensures we resolve the Maxwellian distribution, as well as the escaping tail.
Basically, we had to solve a first order partial differential equation with four dimensions, which are: one for space and one for each of the three velocity components in cartesian coordinates. The results derived when solving for the distribution of particules allow us to compute macroscopic variables that can be used to derive atmospheric properties, such as the number density

$$n(t,r) = \sum_i f(t, v_i, r)(\Delta v)^3 \tag{3.8}$$

the temperature

$$T(t,r) = \frac{m}{3k_b}\left[\frac{1}{n}\sum_i f(t, v_i, r)\vec{v_i}^2(\Delta v)^3 - \vec{u}(t,r)^2\right] \tag{3.9}$$

the bulk velocity component

$$\vec{u}(t,r) = \frac{1}{n}\sum_i f(t, v_i, r)\vec{v_i}(\Delta v)^3 \tag{3.10}$$

the heat flux

$$\vec{q}(t,r) = \frac{m}{2}\sum_i f(t, v_i, r)\vec{v_i}(\vec{v_i} - \vec{u}(t,r))^2(\vec{v_i} - \vec{u}(t,r))(\Delta v)^3 \tag{3.11}$$

or the escape flux

$$F_{esc}(t,r) = \sum_i v_i f(t, v_i, r)(\Delta v)^3 \tag{3.12}$$

for the molecular escape flux, the sum is performed only for particles having a velocity magnitude equal or greater than the escape velocity and directed upwards.

To tackle down the problem, we divided it into one part for each of the two sides of the equation. The left-hand side represents a free molecular flow under a gravitational field, given by the third term, where the particles are free to move between different layers of the space dimension, given by the second term, and do not experience collisions. The right-hand side is called the collision integral and represents the collisions that the particles experience through their motion in time. These collisions eventually affect the motion of the particles in the atmosphere when coupled

with terms of left-hand side. We thus chose to start to work on the left hand side; to be cautious and not to rush into an overwhelming problem, we decided to build a model step by step going up with the dimensions. This way, we could easily identify and go back to any source of mistake when adding content to the code.
Then, we worked on the right-hand side of the equation. This piece of the model was complex and required some time to implement in a code. This is due to the complexity of using discrete velocity method which appeared when trying to compute the collision integral of the non-linear Boltzmann equation. We needed to compute the number of outcomes, from a collision between two particles, that fall on the velocity space grid as well as the redistribution of the velocity vectors of these particles. This complex task is also detailed in the following section. We eventually coupled this discrete collision term with the four-dimensional model and we were able to start comparing our results to those presented in (Merryfield and Shizgal, 1994).

3.1 Development of the Model: a step-by-step process

Here we detail each development step along with the trials we experimented during this building process that helped us decide which techniques we used for the complete problem, from the one-dimensional free molecular flow model to the full model comprising the four dimensions and collisions.

3.1.1 One-Dimensional Free Molecular Flow Model

We started from the one-dimensional case of the Boltzmann equation, which we took to be the radial spatial dimension, using the Maxwell-Boltzmann distribution as the initial condition

$$\frac{\partial f}{\partial t} + v_z \frac{\partial f}{\partial r} - \frac{GM}{r^2} \frac{\partial f}{\partial v_z} = 0 \tag{3.13}$$

Where we need to use the exact solution of the derivative with respect to v_z which allows to have

$$\frac{\partial f}{\partial t} + v_z \frac{\partial f}{\partial r} - \frac{GMmv_z}{kTr^2} f = 0 \tag{3.14}$$

Choosing a constant value for v_z gives us an equation in one dimension. Furthermore, we integrate the equation over v_z to obtain the equation as a function of the number density and not the velocity distribution using the relation

$$\int f(\vec{r}, \vec{c}, t) d\vec{c} = n(\vec{r}, t) \tag{3.15}$$

We then obtain

$$\frac{\partial n}{\partial t} + v_z \frac{\partial n}{\partial r} - \frac{GMmv_z}{kTr^2} n = 0 \tag{3.16}$$

This equation is representative of the hydrostatic relation for a single velocity component and we use it solely to illustrate the effects of upwind schemes and radial resolution.

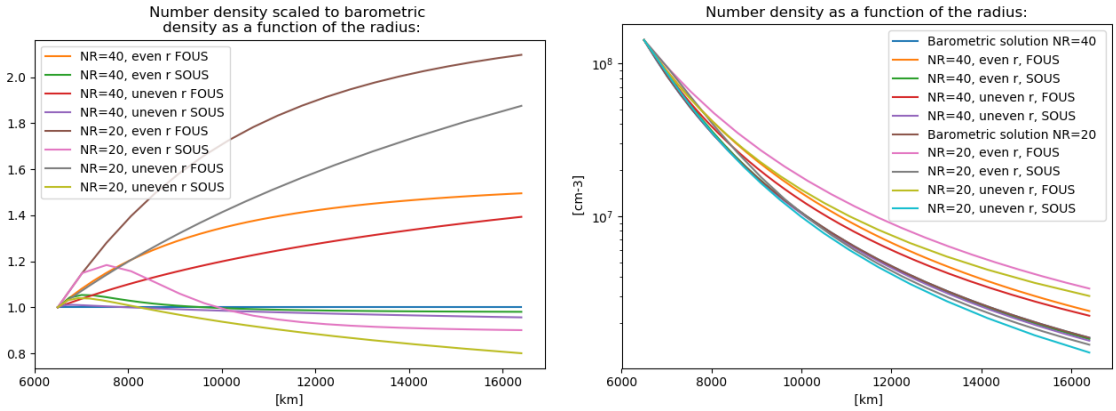

(a) (b)

Figure 3.1: Number density as a function of r after 16 400s with $v_z = 1.0$ km . s^{-1}. The figures show eight different cases described in the plots' legends. Where NR is the number of points in the r grid: Figure (a) is scaled to the barometric solution. Figure (b) is on a logarithmic scale for the number density. SOUS stands for *second-order upwind scheme* and FOUS for *first-order upwind scheme*.

Upwind Scheme

To solve this partial differential equation we used finite difference for the derivative in r. We specifically used an upwind scheme, which uses information from positions where the particles come from in their upward/downward motion. This means that for particles going upwards we will use information from positions below, so we need to use a backward difference scheme, as when particles come from above, we will use forward difference scheme. The formulas for approximating the r derivatives using these schemes are as follows (Inamuro and Sturtevant, 1990)

$$\begin{cases} \dfrac{\partial f(r_s)}{\partial r} \approx \dfrac{f(r_s) - f(r_{s-1})}{\Delta r}, \text{for } v_z > 0 \\ \dfrac{\partial f(r_s)}{\partial r} \approx \dfrac{f(r_{s+1}) - f(r_s)}{\Delta r}, \text{for } v_z < 0 \end{cases} \tag{3.17}$$

to first order and

$$\begin{cases} \dfrac{\partial f(r_s)}{\partial r} \approx \dfrac{3f(r_s) - 4f(r_{s-1}) + f(r_{s-2})}{2\Delta r}, \text{for } v_z > 0 \\ \dfrac{\partial f(r_s)}{\partial r} \approx \dfrac{-3f(r_{s+2}) + 4f(r_{s+1}) - f(r_s)}{2\Delta r}, \text{for } v_z < 0 \end{cases} \tag{3.18}$$

to second order, where Δr is the constant interval in radial space between consecutive radial grid points and s is a subscript representing a radial grid point.

Non-homogeneous Spatial Grid

Merryfield and Shizgal (1994) adopted an uneven grid spacing for the spatial dimension. Using the following relation

$$\lambda(r) = \frac{r}{H(r)} \tag{3.19}$$

if we wish to have a grid distributed uniformely with respect to the Jeans parameter, we have to use the inverse of the variable r. It is introduced in order to have an r spacing that increases as the local scale height increases. Indeed, at low altitudes as the atmosphere changes faster than at higher altitudes because of the smaller scale height, a finer grid is more appropriate, which means more points in order to evaluate the derivatives more accurately. As the scale height increases with altitude and thus properties change more slowly, less grid points are required. Using the inverse r definition to have an uneven grid, permits it. Although, the definition of the upwind scheme needs to be adapted as follows

$$\begin{cases} \dfrac{\partial f(r_s)}{\partial r} \approx \dfrac{(2h_{s-1}h_{s-2}+h_{s-2}^2)f(r_s)-(h_{s-1}+h_{s-2})^2 f(r_{s-1})+h_{s-1}^2 f(r_{s-2})}{h_{s-1}h_{s-2}(h_{s-1}+h_{s-2})}, \\ \qquad\qquad \text{for } v_z > 0 \\ \dfrac{\partial f(r_s)}{\partial r} \approx \dfrac{-(2h_s h_{s+1}+h_{s+1}^2)f(r_s)+(h_s+h_{s+1})^2 f(r_{s+1})-h_s^2 f(r_{s+2})}{h_s h_{s+1}(h_s+h_{s+1})}, \\ \qquad\qquad \text{for } v_z < 0 \end{cases} \tag{3.20}$$

for second order. First order is the same as even grid except the denominator is not constant. Where h_s, h_{s+1} and h_{s-1} are the non-constant intervals in radial space and defined as

$$\begin{aligned} r_{s+1} &= r_s + h_s,\ r_{s+2} = r_s + h_s + h_{s+1},\ \text{for } v_z < 0 \\ r_{s-1} &= r_s - h_{s-1},\ r_{s-2} = r_s - h_{s-1} - h_{s-2},\ \text{for } v_z > 0 \end{aligned}$$

and s is a subscript representing a radial grid point.

For this case we used backward upwind scheme as we had a constant positive v_z. Results of this model can be found in Figure 3.1. We compare different combinations, with the number of points in r being twenty or fourty and also either using even or uneven grid in r. We used as a reference, the barometric number density solution given by

$$n(r) = n_0 \exp\left[\frac{r}{H(r)} - \frac{R}{H(R)}\right] \tag{3.21}$$

for which the repartition of particles does not change with time for free molecular flow. n_0 is the number density at altitude 0 in the simulated atmosphere and was chosen to be $1.417 \times 10^8 \text{cm}^{-3}$, R is the radius at altitude 0 and is equal to Earth's radius and H is the scale height. From Figure 3.1 a, we can clearly state that the use of the second-order upwind scheme is much more consistent with respect to the barometric solution. The use of the fourty points in r also helped to reach a better accuracy. Finally, the use of the uneven grid improves the model at low altitudes as expected and is only a little bit less efficient at high altitudes with respect to the even case.

3.1.2 Two-Dimensional Free Molecular Flow Model

For the following step, we used a two-dimensional case where we let unchanged the derivative with respect to v_z in order to solve it numerically.

$$\frac{\partial f}{\partial t} + v_z \frac{\partial f}{\partial r} - \frac{GM}{r^2} \frac{\partial f}{\partial v_z} = 0 \tag{3.22}$$

Boundary Conditions

Concerning the boundary conditions, we separated the velocity space in two different classifications: one where the particles have a $v_z < 0$ and one where the particles have a $v_z > 0$.
For the lower boundary in r , particles going upwards have the value of the Maxwell distribution, because we considered below this level all particles have this distribution

$$f(r_{min}, v_z, t) = f_{eq}(r_{min}, v_z), \text{ for } v_z > 0 \tag{3.23}$$

First, the simulations were done with a single boundary condition on the particles having a negative z component, without considering escape; that is specular reflections

$$f(r_{max}, -v_z, t) = f(r_{max}, v_z, t), \text{ for } v_z > 0 \tag{3.24}$$

Which means that the particles that were going upward would come back with a velocity of the same magnitude, but with opposite direction. Henceforth, populating the distribution made of the particles with negative component in z. Therefore, the information will propagate from the lower boundary with upward moving particles due to the upwind. Once it gets to the upper boundary, the information propagates back with the downard moving particles down to the lower boundary.

For this two-dimensional case we tried three different options.
The first one tried to solve the equation using the upwind scheme as before and centered difference for the derivative with respect to v_z. However, this method produced unrealistic results. In Figure 3.2, we compare numerical derivative and analytical derivative of Maxwell distribution with respect to v_z. We clearly see a large error in the numerical derivative. This is due to the large variation in f with v_z. This error has an impact strong enough to make the solution wrong after a few integration time steps.

To compensate for this, Merryfield and Shizgal (1994) introduced a prefactor in order to obtain more reasonable results. It is defined by writing

$$f = f_p f_{eq} \tag{3.25}$$

The actual distribution is written in terms of a deviation from the equilibrium distribution, defined in Appendix A, through a prefactor which was equal to 1.0 at time $t = 0$s. In this option, we used this form only for the term containing the velocity derivative. We applied the product rule, obtaining a derivative in v_z over f_p and one over f_{eq} of which we can derive the exact derivative to use for the

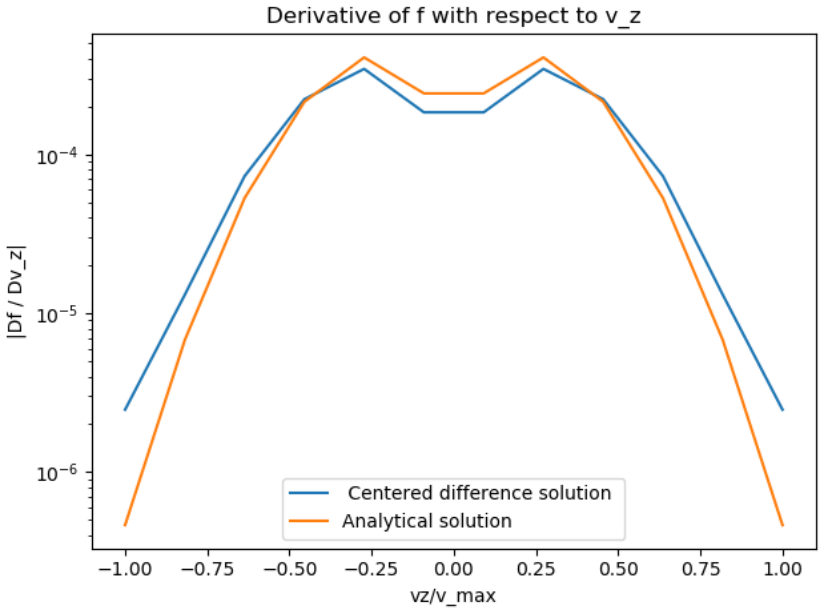

Figure 3.2: Comparison between the analytical derivative and the centered difference approximation of Maxwell's distribution at ground level.

computation of the partial differential equation as follows

$$\frac{\partial f}{\partial t} + v_z \frac{\partial f}{\partial r} - \frac{GM}{r^2} \frac{\partial f_{eq}}{\partial v_z} f_p - \frac{GM}{r^2} f_{eq} \frac{\partial f_p}{\partial v_z} = 0$$

$$\frac{\partial f}{\partial t} + v_z \frac{\partial f}{\partial r} + \frac{GM}{r^2} \frac{m v_z}{kT} f_p f_{eq} - \frac{GM}{r^2} f_{eq} \frac{\partial f_p}{\partial v_z} = 0 \tag{3.26}$$

Part of the equation is thus expressed with an exact analytical solution and allows to reduce total numerical errors.
The third option was by using this prefactor on all three terms of the equation. Figure 3.3 shows results where we simulated the case with uneven r grid, fourty r points, second-order upwind scheme for the previously described second and third option. The improved accuracy of using the prefactor in the distribution for each term is clearly visible. Indeed, for the free molecular flow, the evolution with time of a Maxwellian distribution should stay close to a Maxwellian. We see that when we compare our solution f with the equilibrium distribution f_{eq} it is not greatly diverging from 1.0 when we use the prefactor. We thus consider the use of this prefactor to be efficient.

Escape Boundary Conditions

In order to simulate the escape, we applied the same boundary condition as earlier, except that for particles going up with a velocity component in z having a velocity magnitude greater than the escape velocity, we applied a different condition as follows

$$f(r_{max}, -v_z, t) = \alpha(t) f(r_{max}, v_z, t), \text{ for } v_z > 0, \; v \geq |\vec{v}_{esc}| \tag{3.27}$$

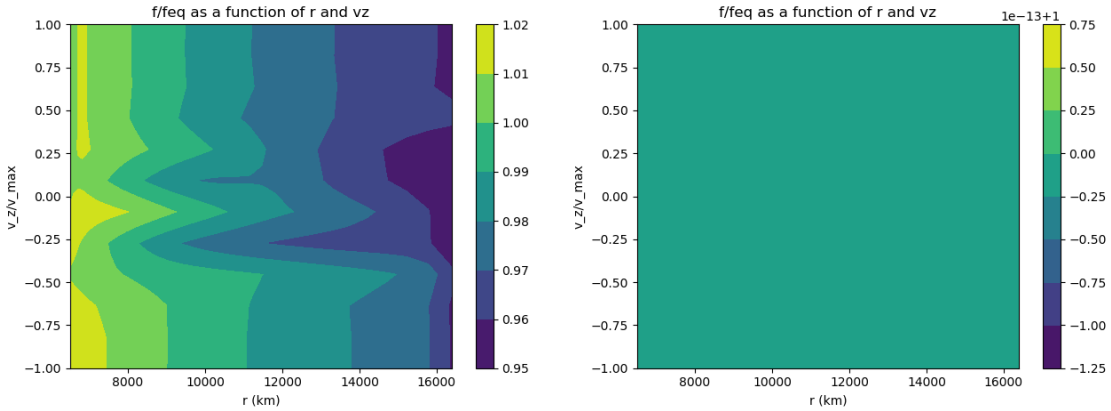

(a) (b)

Figure 3.3: Distributions $f(v_z, r)$ scaled to $f_{eq}(v_z, r)$ as a function of r and v_z scaled to v_{max} after 16 400s with 40 grid points in r and 12 in v_z for the two-dimensional model with $\alpha = 1$. Both use uneven r grid and second-order upwind scheme, (a) prefactor only in the derivative with respect to v_z;(b) prefactor used in all terms.

$$f(r_{max}, -v_z, t) = f(r_{max}, v_z, t), \text{ for } v_z > 0, \ v < |\vec{v}_{esc}| \tag{3.28}$$

with

$$\alpha(t) = \frac{1}{2}\left[1 - \tanh\left(\frac{t}{2000} - 3\right)\right] \tag{3.29}$$

which means that the distribution of particles with a negative z velocity component with a magnitude greater than the escape velocity, will not be replenished at the upper boundary anymore. This effect is observed in Figure 3.6 for example, where the distribution for negative value of v_z starts to have values equal to zero.
The role of α is to activate gradually this second boundary condition. Indeed, as time goes the value of α tends to zero. The reason for having this gradual change towards zero is explained by Merryfield and Shizgal (1994) by the fact that turning the boundary condition 3.27 immediatly on, would induce an artificial phenomenon of transient acoustic waves in the results. They thus found that this value of α allows to avoid the phenomenon in the results and we decided to apply it as well in the model.

Finally, the introduction of the escape condition induced some oscillations in the results. They come from the presence of the discontinuity between the depleted part of the velocity distribution and the part non affected by the condition. The second-order centered scheme probably uses too few points and instability is generated because of the values being too extreme in this region. In an attempt to reduce the peaks of these oscillations, we tried approximating the derivative with respect to v_z using fourth-order centered differences but only for the option of the second two-dimensional case using the prefactor in all the terms. See Figure 3.4. The impact of the fourth-order was to flatten the peaks, but also to increase their number, we chose to use the second-order centered difference as the fourth-order did not substantially change results. An other possibility that should be investigated is the use of virtual viscosity, that could smooth out the peaks although we have not taken time for this option.

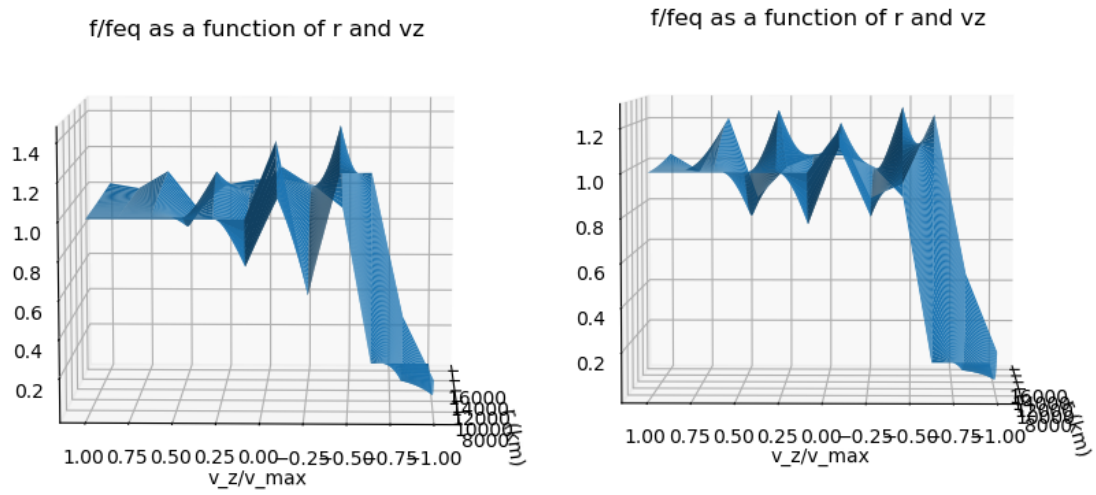

(a) (b)

Figure 3.4: Distributions $f(v_z, r)$ scaled to $f_{eq}(v_z, r)$ as a function of r and v_z scaled to v_{max} after 16 400s with 40 grid points in r and 12 in v_z for the two-dimensional model using the prefactor and with α activated. Both figures use uneven r grid and second-order upwind scheme: (a) second-order and (b) fourth-order centered difference on the derivative with respect to v_z. The third axis is the r axis and is the same as for the others, the picture is oriented this way for more clarity.

3.1.3 Choice of Solving Schemes for the Derivatives

During the development of the model, we tested a series of options for the finite difference schemes that we used to approximate the derivatives in order to find out which combinations were more accurate for solving. To do so, we used a series of variables which were: even or uneven grid in r, number of points for the spatial coordinate as well as the order for the upwind scheme. The finite difference scheme used for the derivatives with respect to v was set to the centered second-order as explained earlier, as higher orders did not change the results in a significant way. The results of these different combinations are showed in the different plots in this section. The one-dimensional case is given in Figure 3.1 where we notice the effect of the order of the upwind scheme on the solution. The first-order cases show a significant departure from the barometric value compared to the second-order cases. Uneven r grids and increased number of points seem to also produce solutions that are closer to the barometric solution.
Figures 3.3, 3.5 and 3.6 confirm these choices and the better performance of second-order upwind scheme in combination with uneven r grids.
As noted above, the use of the prefactor in each term improves the accuracy of the results and this is why, from then on, we chose to use exclusively these specific parameters for the next development steps of the model.

3.1.4 Four-Dimensional Model

For this stage the x and y components of the velocity are also taken into consideration. Accordingly, our model is now based upon the following four-dimensional

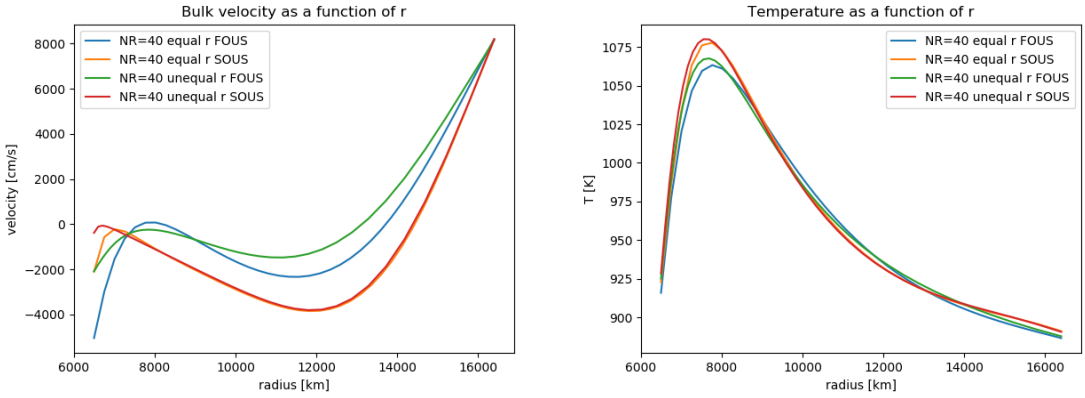

(a)

(b)

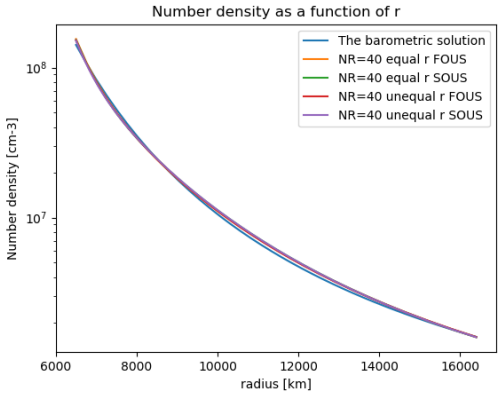

(c)

Figure 3.5: Different macroscopic variables computed for four different cases after 16 400s with 40 grid points in r and 12 in v_z for the two-dimensional model using the prefactor and with α activated: (a) bulk velocity; (b) temperature. (c) number density along with the barometric solution. SOUS stands for *second-order upwind scheme* and FOUS for *first-order upwind scheme*.

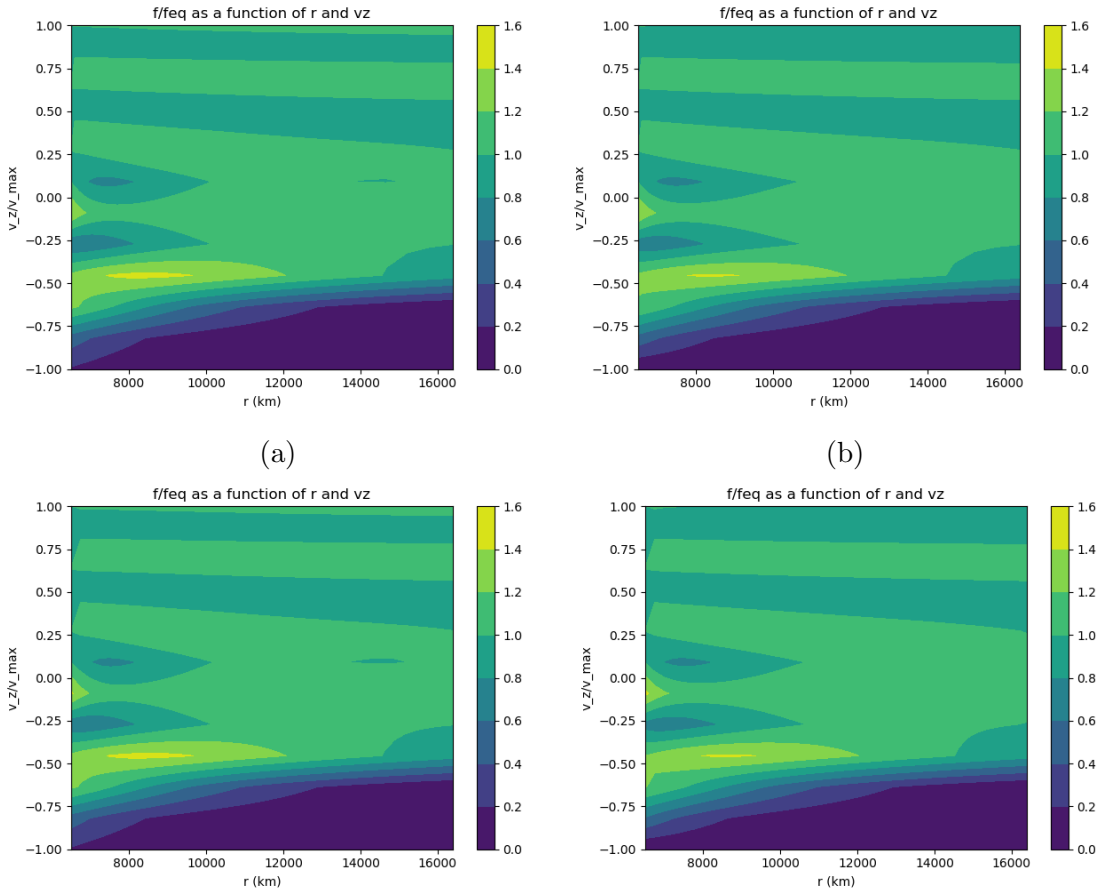

Figure 3.6: Distributions $f(v_z, r)$ scaled to $f_{eq}(v_z, r)$ as a function of the radius and v_z scaled to v_{max} after 16 400s with 40 grid points in r and 12 in v_z for the two-dimensional model using the prefactor and with α activated: (a) uneven r grid and second-order upwind scheme; (b) uneven r grid and first-order upwind scheme; (c) eve, r grid and second-order upwind scheme; (d) even r grid and first-order upwind scheme.

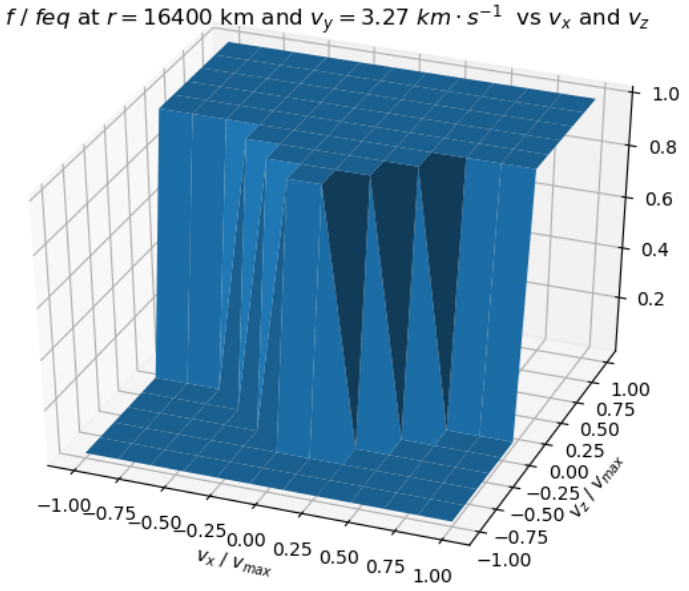

Figure 3.7: Distribution after 16 400s scaled to the equilibrium distribution. We used second-order upwind scheme for the derivatives with respect to r with fourty grid points on an uneven grid. α is activated.

equation

$$\frac{\partial f}{\partial t} + c_z \frac{\partial f}{\partial r} - \frac{1}{r}\left[c_x c_z \frac{\partial f}{\partial c_x} + c_y c_z \frac{\partial f}{\partial c_y} - (c_x^2 + c_y^2)\frac{\partial f}{\partial c_z}\right] - \frac{GM}{r^2}\frac{\partial f}{\partial c_z} = 0 \tag{3.30}$$

For this case we also applied the factorisation $f = f_p.f_{eq}$ on all the terms. We still used second-order centered differences for the derivatives with respect to velocity and the second-order upwind scheme for the derivative with respect to r. The solution to the use of the prefactor in the full four-dimensional equation can be found in Appendix A. In Figure 3.7 we display the result of the four-dimensional free molecular flow model solved with uneven grid for r and the parameters mentioned at the end of the previous subsection. The effect of α is clearly visible in the lower half of the v_z component where the distribution has been depleted as a result of the particles' escape and the boundary condition 3.27.

3.1.5 Discretised Collision Term

In order to complete the model, we needed to work on the last step which was to add the collisions to the four-dimensional free molecular flow model. First, we have worked on the collision integral separately and when computed we eventually added it to the model. The main sources of our understanding on how to build this discretised collision integral come from (Inamuro and Sturtevant, 1990) and (Merryfield and Shizgal, 1994).
The collision integral of the non-linear Boltzmann equation is given as

$$\int\int [f_1' f_2' - f_1 f_2]\sigma(g, \Omega) g d\Omega dc_2 \tag{3.31}$$

In its discretised form, it is written as

$$\sum_{j=1}^{p} \sum_{k,l} A_{ij}^{kl} (f_k f_l - f_i f_j) \cdot \Delta v^3. \tag{3.32}$$

It actually translates the collisions between pairs of identical particles and considers them as hard spheres. For more details regarding the derivation of the discretised form, please refer to Appendix B. Here, we detail how to implement each term of this formula.
The terms inside parantheses are the production and loss term; as described in the section about Boltzmann collision integral in Chapter 2, a test particle having random velocity vector i, from the velocity space, can collide with any other particle presenting a velocity vector denoted by index j from the chosen velocity space. The sum over j bears this information by summing over the number p of velocity vectors forming the space minus the vector i [1]. This finite number p is the total number of discrete velocities. Therefore, if NV_x, NV_y, NV_z are the number of points along the x, y and z velocity axes respectively, then the number of possible velocity vectors in the space is equal to $NV_x \cdot NV_y \cdot NV_z$. In our model we chose to give each coordinate the same number of points to facilitate the computations. We tried the same combinations as in (Merryfield and Shizgal, 1994), that is either 12, 14 or 16 points along each velocity axis.
As mentioned before, the number of points along with the range of velocity will determine the resolution of our velocity space. This resolution is given by Δv, the velocity step. As we had to resolve the Maxwell distribution, that is having a step smaller than its standard deviation given in Equation 3.7 and equal to 2.87 km.s^{-1}, if we choose $T_0 = 1\,000$K, we decided to choose the same value as in (Merryfield and Shizgal, 1994) for our maximum velocity which is $v_{max} = 12$ km.s^{-1}. In this way, our largest step is when we consider 12 points and thus equals 2 km.s^{-1}, the distribution is then fairly resolved. In the meantime, following again the values from Merryfield and Shizgal (1994), the escape velocity given in Equation 3.6 is equal to 9.4 km.s^{-1} at the exobase and 7.0 km.s^{-1} at the maximum altitude of the model, chosen to be 16 400 km. Thus, the value 12 km.s^{-1} for the maximum velocity allows to cover the escape velocity and therefore assure that certain particles will display a velocity greater than the escape velocity.
We can visualise this discrete space as a three-dimensional grid directed by the axis of the Cartesian velocity coordinates. Each grid node represents a velocity vector composed of three coordinates. To help visualise this space we show a two-dimensional representation of the velocity space in Figure 3.8 that we adapted from (Dimarco and Pareschi, 2014). Furthermore, this grid is placed in such a manner that it is staggered with respect to the Cartesian axes and falls on an half integer value of a coordinate. This choice has been justified by Inamuro and Sturtevant (1990) based upon the fact that it helps avoiding errors at the boundaries of the spatial grid.
Moreover, we neglect internal energy, which implies that when two particles collide there is conservation of mass, momentum and also energy. Therefore, the magnitude

[1] It is assumed that a particle with a velocity vector i cannot collide with an other particle with the same velocity vector. Furthermore, this choice was encouraged by the fact that the collision integral would be zero as the coefficient $A_{ij}^{kl} = 0$.

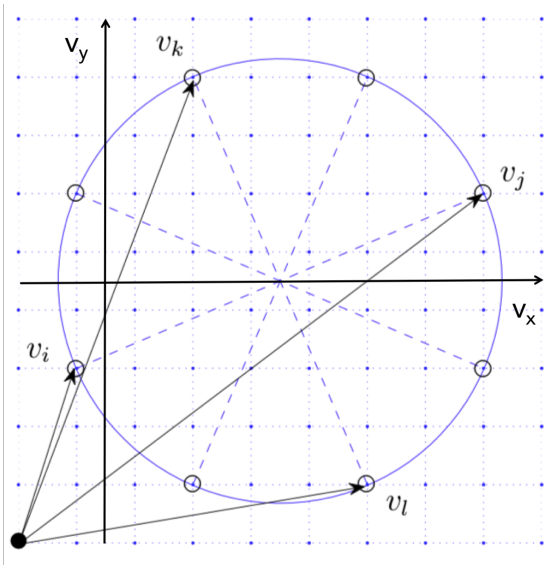

Figure 3.8: Two-dimensional representation of the velocity grid or discrete velocity space with a sketch of a velocity pair of particles and its collision outcomes. Each pair is centered on the center of momentum of the colliding particles, (Dimarco and Pareschi, 2014).

of the relative velocity between the two outcome particles is the same as between v_i and v_j and these two new vectors must have their center of momentum corresponding to the pre-collision center of momentum. We thus obtain a sphere drawn by the redistribution of the outcomes around this center of momentum. However, only the pairs of outcomes falling on one intersection between the sphere and the grid are considered for the model. This is shown in Figure 3.8 where we see that the pair $(v_i,\ v_j)$ has eight outcomes meeting the requirements in this considered plane, since permutations (k, l) and (l, k) are in fact different outcomes. The first term in paranthesis represents the velocity distribution functions of one possible outcome of the collision between particle i and j, this is why we need to sum over k and l to take into account all the outcomes. Although, we talk about this term as representing outcomes, but as explained in Chapter 2, this is in fact the inverse collision of i and j so this term is formed by the velocity distribution functions of pairs of velocity vectors which could form the initial (i, j) pair after a collision.
The most complicated part was to record for each velocity vector combinations, their respective number of outcomes, which appears in the coefficient A_{ij}^{kl} as C_{ij}, as well as their identity (to compose a correct distribution). This part of the code is also the most time consuming as we need to loop through $NV^6 - NV^3$ combinations in order to record all the outcomes. This required between 2 984 256 and 16 773 120 combinations. Fortunately, this action is performed once at the beginning of the run, however, we stil had to loop through NV^3 steps to account for each velocity element of the distribution in order to thoroughly investigate the whole velocity distribution. Finally, this latter loop had to be performed for each slab in atlitude, we can thus multiply by the number of points on the spatial coordinate. In total, for each time step, we needed to compute the time dependent solution of Equation 3.2 between 34 560 and 81 920 times for twenty spatial points and between 69 120 and 163 840 times for fourty spatial points.

3.2 Solving the Equation

A few tricks were used to solve the equation of the complete model and they are described in this section .
Let us start with the following relation derived in the Appendix A were we used the prefactor in the velocity distribution function:

$$\left[\frac{\partial f_p}{\partial t} + v_z\frac{\partial f_p}{\partial r} - \frac{1}{r}\left[v_x v_z\frac{\partial f_p}{\partial v_x} + v_y v_z\frac{\partial f_p}{\partial v_y} - (v_x^2+v_y^2)\frac{\partial f_p}{\partial v_z}\right] - \frac{GM}{r^2}\frac{\partial f_p}{\partial v_z}\right] = \frac{C[f]}{f_{eq}} \tag{3.33}$$

First, we rewrite the right-hand side as

$$C[f] = P[f] - L[f] \tag{3.34}$$

where,

$$P[f] = \sum_{j=1}^{p}\sum_{k,l} A_{ij}^{kl} f_k f_l \cdot \Delta v^3 \tag{3.35}$$

$$L[f] = \sum_{j=1}^{p}\sum_{k,l} A_{ij}^{kl} f_i f_j \cdot \Delta v^3. \tag{3.36}$$

We also write the terms with velocity derivatives as

$$\vec{d}\cdot\nabla_v f \tag{3.37}$$

where,

$$\vec{d} = \left\{\frac{v_x v_z}{r}, \frac{v_y v_z}{r}, \frac{-(v_x^2+v_y^2)}{r} + \frac{GM}{r^2}\right\}. \tag{3.38}$$

Formally, Equation 3.33 becomes

$$\frac{\partial f_p}{\partial t} + v_z\frac{\partial f_p}{\partial r} - \vec{d}\cdot\nabla_v f_p = \frac{P[f]-L[f]}{f_{eq}}. \tag{3.39}$$

Merryfield and Shizgal (1994) used a combination of two integration schemes to solve this equation. The first one was the second-order implicit Crank-Nicolson scheme on the second term of the collision part. For the remaining terms an explicit second-order Adams-Bashford was adopted. Accordingly Equation 3.39 becomes

$$\frac{f_p(t+\Delta t) - f_p(t)}{\Delta t} + \frac{1}{2}\frac{L[f(t+\Delta t)]}{f_{eq}} + \frac{1}{2}\frac{L[f(t)]}{f_{eq}} = \frac{3}{2}S(t) - \frac{1}{2}S(t-\Delta t) \tag{3.40}$$

where,

$$S(t) = -v_z\frac{\partial f_p(t)}{\partial r} + \vec{d}\cdot\nabla_v f_p(t) + \frac{P[f(t)]}{f_{eq}} \tag{3.41}$$

The terms in the sum of Equation 3.36 do not directly depend on the indices k and l, thus the sum becomes

$$L[f] = C_{ij}\sum_{j=1}^{p} A_{ij}^{kl}(f_i f_j)\cdot\Delta v^3 \tag{3.42}$$

where C_{ij} is the number of outcomes from the collision between particles of velocity vectors i and j and whose value depends on each different pairs. Further, the term f_i can be factored out, we therefore have

$$L[f] = f_i.A = f_i C_{ij} \sum_{j=1}^{p} A_{ij}^{kl} f_j \cdot \Delta v^3 \tag{3.43}$$

We thus only obtain a vector of size $NV3$ and not a matrix of size $NV3 \times NV3$. We rewrite 3.40 as

$$\begin{aligned} \frac{I f_p(t+1)}{\Delta t} - \frac{I f_p(t)}{\Delta t} + \frac{1}{2}\frac{A(t+1)f_i(t+1)}{f_{eq}} + \frac{1}{2}\frac{A(t)f_i(t)}{f_{eq}} &= \frac{3}{2}S(t) - \frac{1}{2}S(t-1) \\ \frac{I f_p(t+1)}{\Delta t} + \frac{1}{2}\frac{A(t+1)f_i(t+1)}{f_{eq}} &= \frac{I f_p(t)}{\Delta t} - \frac{1}{2}\frac{A(t)f_i(t)}{f_{eq}} + \frac{3}{2}S(t) - \frac{1}{2}S(t-1) \end{aligned} \tag{3.44}$$

where I is the vector identity and A a vector of size $NV3$. As mentioned in Section 3.1.3, the derivatives with respect to r are evaluated using second-order upwind schemes and the derivatives with respect to v with second-order centered difference scheme. We rearrange the terms to obtain

$$\left(I + \frac{\Delta t}{2}A(t+1)\right) f_p(t+1) = \left(I - \frac{\Delta t}{2}A(t)\right) f_p(t) + \Delta t\frac{3}{2}S(t) - \Delta t\frac{1}{2}S(t-1) \tag{3.45}$$

Nevertheless, the loss term is a product of the distributions f_i and f_j. Also we want to solve only for f_i and not for f_j and thus need information on the value of $f_j(t+1)$, which is not known. Therefore, Merryfield and Shizgal (1994) used a first step using $A(t+1) = A(t)$ to compute an approximation to $f_i(t+1)$. These values are used to update $A(t+1)$ and another step is performed to compute $f_i(t+1)$.

Chapter 4

Results and Discussions

In this section we present the results of a series of simulations where we show the radial profiles of some relevant macroscopic variables, discuss the time evolution and sensitivity to parameters change. Later, we compare the results of the DVM method to the fluid-Jeans method and the DSMC method shared by Dr. Orenthal J. Tucker (for example (Tucker and Johnson, 2009)).

As showen in Merryfield and Shizgal (1994), we have done four principal simulations as followed: the first one used twelve velocity points with twenty radial points, the second one used fourteen velocity points with twenty radial points, the third one used sixteen velocity points with twenty radial points and the last one used twelve velocity points and fourty radial points. These simulations are named DVM 1, DVM 2, DVM 3 and DVM 4, respectively, hereafter.

The model uses a lower boundary condition given as

$$f(r_{min}, v_z, t) = f(r_{min}, -v_z, t), \text{ for } v_z > 0 \tag{4.1}$$

we call it *specular* condition. It considers that particles going downward at the lower boundary experience specular reflection. It also imposes that there is no bulk velocity in the atmosphere at the lower boundary.

For this *specular* condition, the CFL condition allowed us to use a 5 sec time step for the first three simulations and a time step of 2.5 sec for DVM 4 in order to have stable solutions. As in Merryfield and Shizgal (1994), the simulation time was 16 000 sec, we thus needed 3 200 and 6 400 steps, respectively, to reach the same time of integration. All the results were simulated for an Earth-like atmosphere meaning we chose to use a mass of 5.97237×10^{27} g for the host body, a radius of $6\,370 \times 10^5$ cm for the radius of the host body, an atmosphere composed of hydrogen molecules, a lower boundary number density of $1.417 \times 10^8 \text{cm}^{-3}$ and an initial temperature of 1 000 K. This placed us in the region of low Jeans parameters, indeed at this lower boundary, Equation 2.9 gives $\lambda_0 \sim 7.57$.
The computation time for the simulations on the high performance computer from BIRA - IASB were recorded for each run. The DVM 1 simulations took an average of 10 hours 20minutes; the DVM 2, an average of 28 hours; the DVM 3, an average of 69 hours and DVM 4, an average of 40 hours. For the longest run, we achieved a reduction in the computation time of a factor more than ten, with respect to

the computation time achieved by Merryfield and Shizgal (1994). Moreover, this computation time could be more reduced by using the presence of symmetry in the computation of the sphere of collision outcomes (Merryfield and Shizgal, 1994). This feature reduced their computation time by about a factor of two. Furthermore, by applying parallelization to the code previously to running it on the hpc, time could also be saved. These features, however, have not been implemented in this work and the code was run in a single thread on the hpc.

4.1 Comparison to Merryfield and Shizgal (1994)

We start by comparing our results to those presented in (Merryfield and Shizgal, 1994) with the macroscopic variables derived from the different simulations. These macroscopic variables are computed using the previously introduced formulas

$$n(t,r) = \sum_i f(t, v_i, r)(\Delta v)^3 \tag{4.2}$$

for the number density,

$$T(t,r) = \frac{m}{3k_b}\left[\frac{1}{n}\sum_i f(t, v_i, r)\vec{v}_i^2(\Delta v)^3 - \vec{u}(t,r)^2\right] \tag{4.3}$$

for the the temperature,

$$\vec{u}(t,r) = \frac{1}{n}\sum_i f(t, v_i, r)\vec{v_i}(\Delta v)^3 \tag{4.4}$$

for the bulk velocity component. The outward molecular rate was computed using the following relation

$$\phi_{out}(t,r) = 4\pi r^2 nu \tag{4.5}$$

Results for the different simulations are presented in Figure 4.1. All the orders of magnitudes match with those from (Merryfield and Shizgal, 1994) and the values are really consistent with each others. We are confident in saying that we reproduced the model correctly.
From Figure 4.1 a, we see that all the number densities are similar, which suggests that the grids are sufficiently fine. We also observe that they are lower than the barometric solution. This is coherent with the decrease of temperature due to escape and the non-isothermal aspect of DVM. At high altitudes where collisions are rare, the hydrostatic equilibrium can no longer be assumed, thus, we can expect a departure from the barometric solution. In Figure 4.1 b, temperature decreases, which is indicative of an ongoing escape cooling the atmosphere. In Figure 4.1 c, we see that the atmosphere has acquired a bulk velocity of about 15 000 cm . s^{-1} at the upper boundary. However, negative values are present below the exobase, located at about 2 500 km in altitude. Merryfield and Shizgal (1994) exlpain this phenomenon as a consequence of the atmosphere's cooling and its tendency to be close to hydrostatic equilibrium in regions below the exobase. In Figure 4.1 d, the outward molecular rate reaches values larger than the Jeans escape rate. Indeed, in our case Jeans escape rate is about 3.38×10^{29} s^{-1} while the outward molecular rate for DVM 1 is about 4.98×10^{29} s^{-1}, meaning that even above the exobase, the

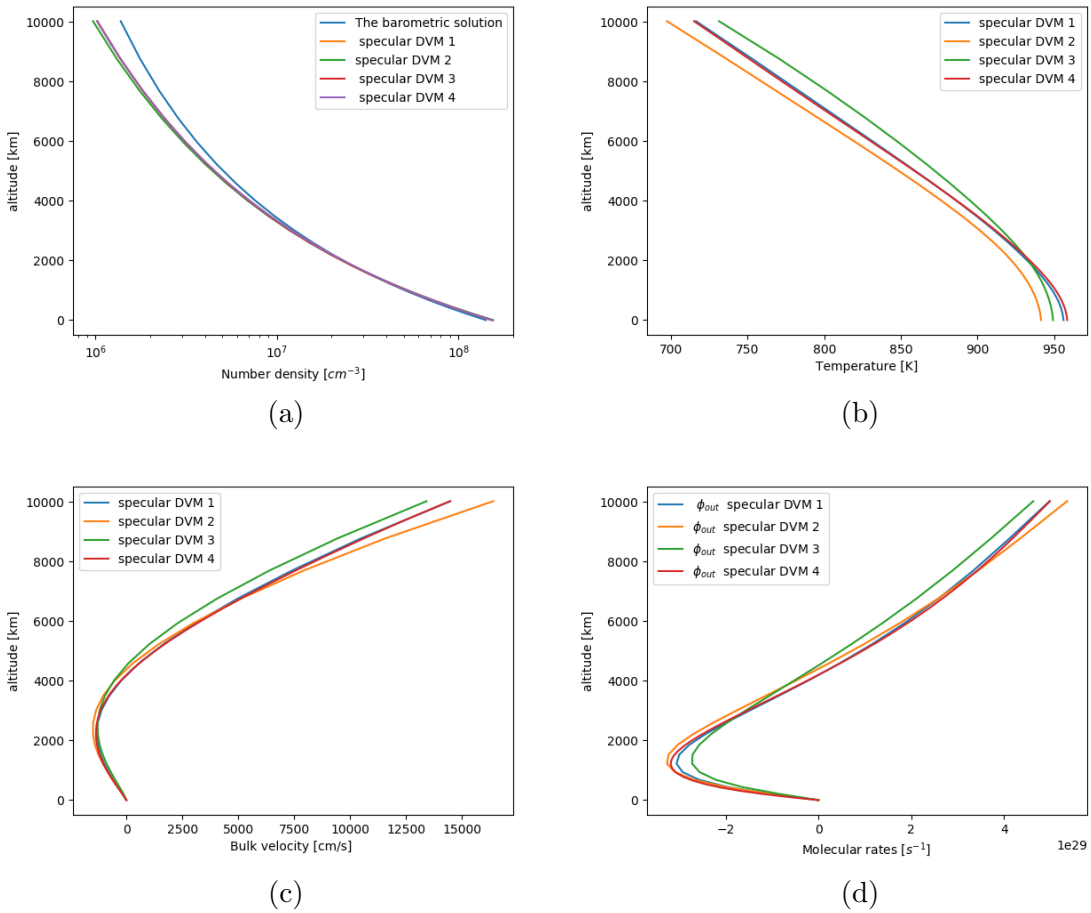

Figure 4.1: Profiles of macroscopic variables vs altitude. Computed after 16 000 s and using the *specular* condition.

outward rate keeps increasing. This suggests that Jeans assumption on the escape rate might underestimate the true value.

We can also observe the velocity distribution of the particles at the end of the simulation at the different radial levels. We have scaled the velocity distribution to the Maxwell-Boltzmann distribution computed using the value of the temperature derived at the end of the simulation and multiplied by the value of the number density at this time. We name this distribution f_s for *scaling distribution function*. This allows to see the departure from a Maxwell-Boltzmann distribution and to visualise what is happening at the boundaries, such as we did in Chapter 3. We show results for 10 030; 5 225; 2 598 and 941 km of altitude in Figure 4.2. However, we used the first positive value of the v_y component, i.e. $v_y = 0.8$ km s^{-1} for the DVM 3 and not $v_y = 0$km s^{-1} as in Merryfield and Shizgal (1994). The extreme values at the corners and some negative values are an apparent consequence of the finite difference schemes inducing numerical errors, in addition with the fact that we divide by really small values of the scaling distribution in these regions. Furthermore, the peaks seen in the negative half of the v_z axis can be attributed to the presence of the discontinuity induced by the upper boundary condition propagating to lower altitudes before being dissipated by collisional relaxation, (see Section 3.1.3). In-

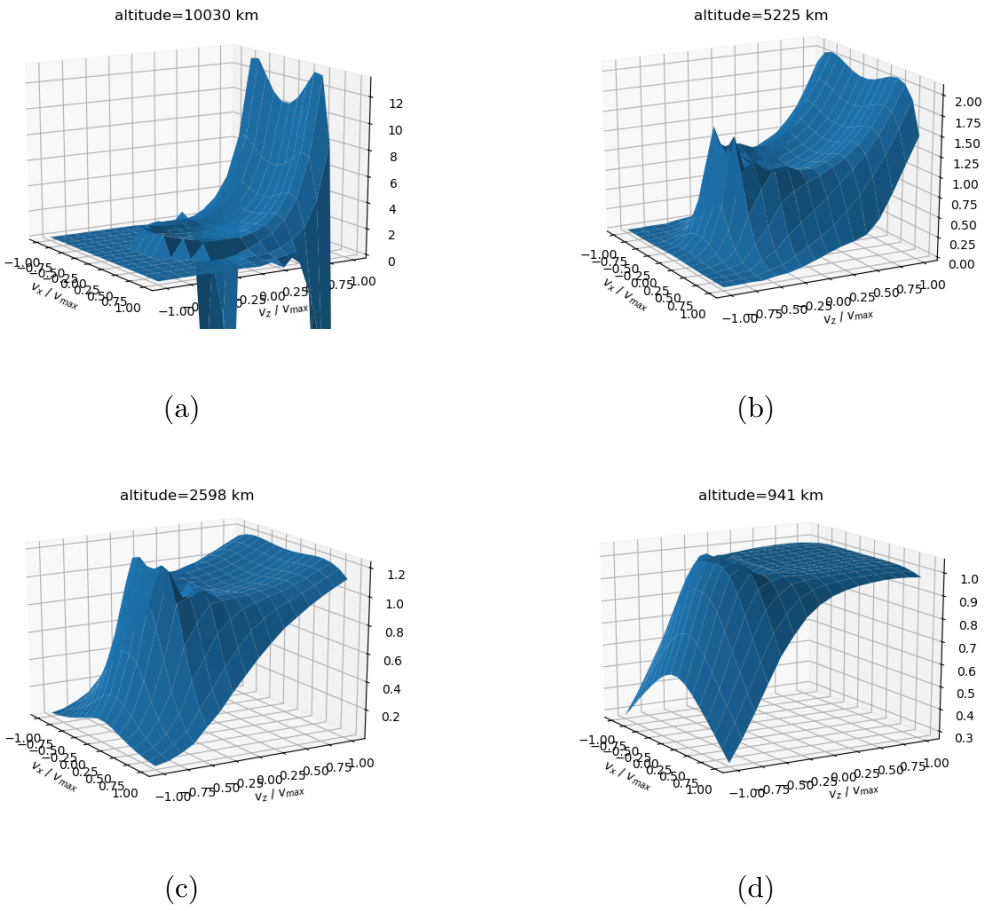

(a) (b)

(c) (d)

Figure 4.2: Three dimensional velocity distribution function as a function of v_z and v_x for $v_y = 0.8$ km s^{-1} for DVM 3 *specular* condition after $t = 16\,000$ s. The function is scaled using the scaling distribution. Velocities are scaled to the maximum velocity of the domain which is 12 km . s^{-1}.

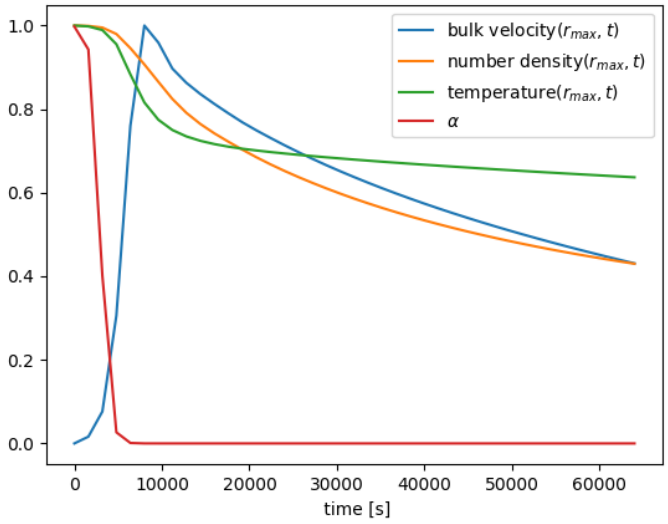

Figure 4.3: Profiles of macroscopic variables and α vs time at the upper boundary for *specular* condition. The variables have been scaled to their maximum values.

deed, we have used a second-order centered finitie difference scheme to evaluate the derivatives with respect to the velocity. This scheme probably uses too few points and instability is generated because of the values being too extreme in this region. As noted in (Merryfield and Shizgal, 1994) this model cannot reach steady state. Therefore, it is interesting to run simulations for a longer time than the time we used for all the first runs in order to see the long term evolution. In these runs we simulated for 64 000 seconds instead of the 16 000 seconds used in (Merryfield and Shizgal, 1994). In Figure 4.3 we confirm that the variables do not reach steady state. This is due to energy leaving the atmosphere with escaping particles and to the fact that the lower boundary is not replenished by new particles. The atmosphere slowly evaporates and cannot reach equilibrium.

4.2 New Lower Boundary Condition

The inconvenience of not reaching a steady state forced us to introduce an alternative lower boundary condition. We call it the *fixed* boundary condition and it considers that the velocity distribution at the lower boundary is the equilibrium distribution as explained in Chapter 3. The *fixed* condition is given by

$$f(r_{min}, v_z, t) = f_{eq}(r_{min}, v_z), \text{ for } v_z > 0 \tag{4.6}$$

and states that the part of the atmosphere above the lower boundary will always be replenished from below as the velocity distribution of particles is held constant there.
The CFL condition allowed to use a 10 sec time step for DVM 1, 2 and 3 and a time step of 2.5 sec for DVM 4. Using the exact same parameters as for the other

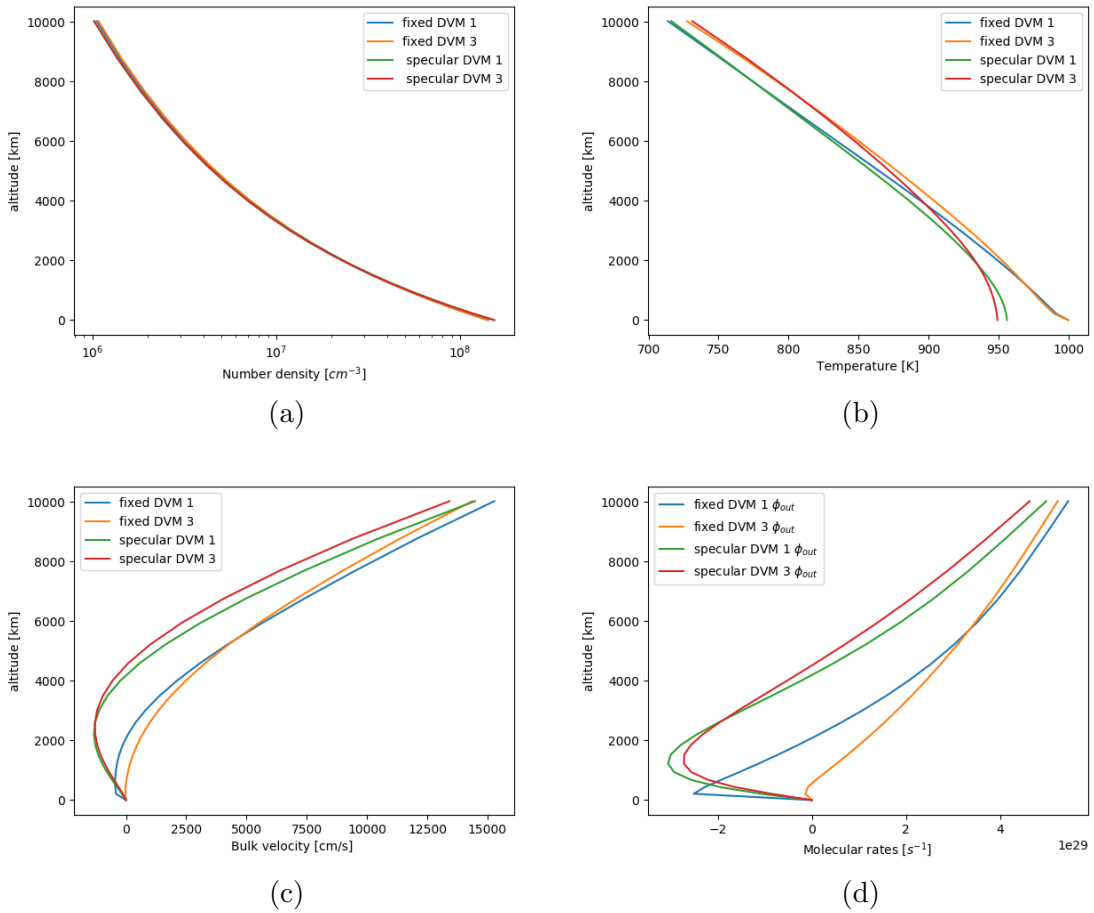

(a) (b)

(c) (d)

Figure 4.4: Profiles of macroscopic variables vs altitude. Computed after 16 000 s and using both conditions.

condition, the computation time for the simulations on the high performance computer were equal in average to: 5 hours 25 minutes for DVM 1; 14 hours for DVM 2; 36hours for DVM 3 and 40 hours for DVM 4. The difference with respect to the first condition is due to the value of the time step.

First, we compare the macroscopic variables computed with the two conditions and this is displayed in Figure 4.4, where we only plotted for DVM 1 and 3 for purposes of visibility. We can see that the results are consistent with each other and in the same range with some interesting exceptions. In Figure 4.4 a, the density derived with the *fixed* condition show a great consistence with those from Merryfield and Shizgal (1994). In Figure 4.4 b, the temperatures are similar at the upper boundary, but the values at the lower boundary stayed much closer to T_0, which is more realistic and expected from the condition. In Figure 4.4 c, the values of bulk velocity are less negative, which is also more realistic. The values at high altitudes are similar to the *specular* condition values. However, at lower boundary, the values are still not consistent with an escaping atmosphere, as we would expect that an atmosphere's bulk velocity at lower boundary to be non-zero. In Figure 4.4 d, DVM 3 shows less negative rates and the values at upper boundary are similar.

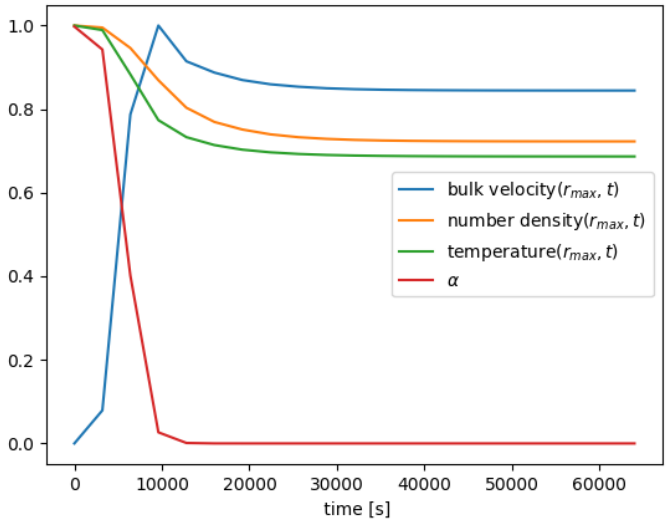

Figure 4.5: Profiles of macroscopic variables and α vs time at the upper boundary for *fixed* condition. The variables have been scaled to their maximum values.

Now, we can look at the values derived from *fixed* condition after 64 000 s. From Figure 4.5 it is clear that steady state can be reached when using the *fixed* condition. In fact, this condition reaches steady state after about 20 000 s, we can thus use the results obtained after 64 000 s in order to be as close to steady state as possible and have more reliable results. In Figure 4.6 a, the densities barely evolved in steady state. In Figure 4.6 b, temperatures have decreased further in steady state as expected. In Figure 4.6 c, the bulk velocity has slightly decreased at the upper boundary compared to the non steady state values. In Figure 4.6 d, the outward rate reaches an almost constant value at the upper boundary, which is consistent with conservation of mass. Indeed, a positive gradient in the outward rate would mean that there should be creation of matter somewhere in the atmosphere below. The rates are not constant at all altitudes because at the lower boundary, the condition forces the atmosphere to be hydrostatic, i.e. $u = 0$.

It is also worth comparing the velocity distribution functions computed using the two conditions. Figure 4.7 shows that the upper tail of the velocity distribution in z is always greater for the *fixed* than for *specular* condition, meaning that there are more particles that can escape in the same amount of time. This is consistent with the values of the outward rates displayed in Figure 4.4 d.

4.2.1 Upper Boundary Value

One other interesting feature to consider is the effect of increasing the value of the upper boundary on the results of the simulations. Lifting the upper boundary means that we consider the limit at which particles will no longer experience collisions to be at a higher altitude. This also increases the value of the Knudsen number at the upper boundary, thus placing us closer to free molecular flow conditions and the results of the escape process will obviously be altered by this action. We have increased the upper boundary to 39 057.3 km in order to at least double its value.

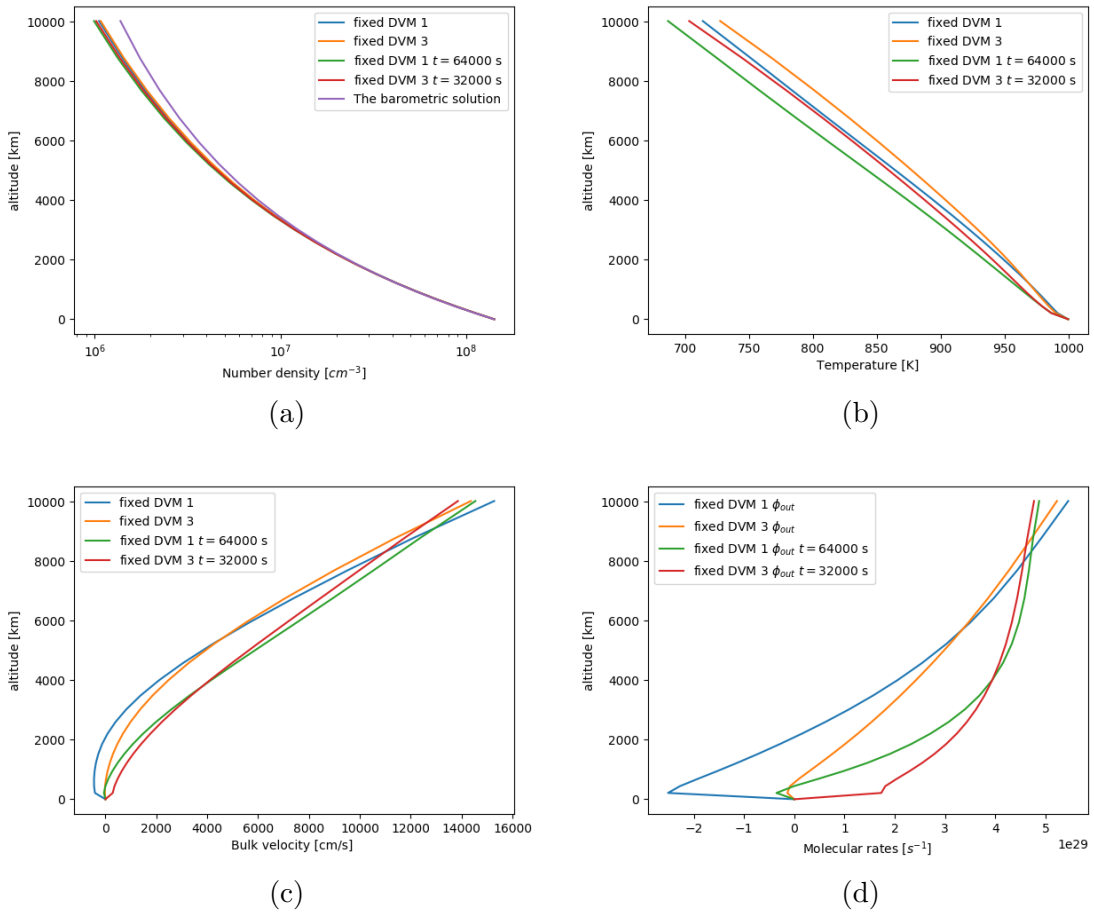

Figure 4.6: Profiles of macroscopic variables vs altitude. Computed using the *fixed* condition. The results for steady state are compared to the other runs of 16 000 s.

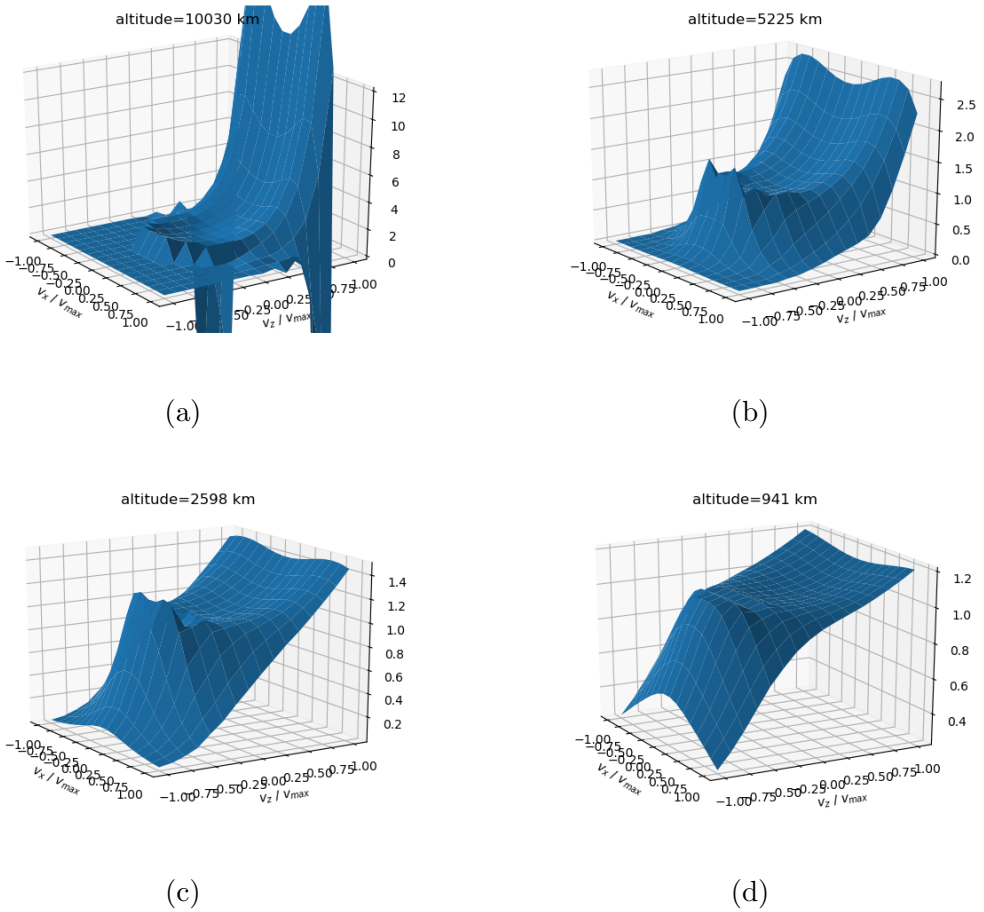

(a) (b)

(c) (d)

Figure 4.7: Three dimensional velocity distribution function as a function of v_z and v_x for $v_y = 0.8$ km . s^{-1} for DVM 3 *fixed* condition after $t = 16\,000$ s. The function is scaled using the scaling distribution. Velocities are scaled to the maximum velocity of the domain which is 12 km . s^{-1}.

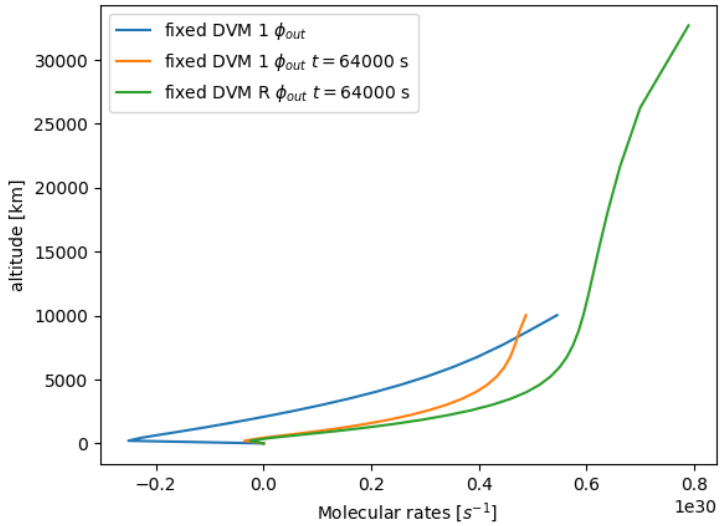

Figure 4.8: Outward molecular rate as a function of altitude for DVM 1 and DVM R at different times. Shows the effect of increasing the value of upper boundary.

We chose this non usual value for r_{max} to have an integer number of radial points and in order to have the same radial grid spacing at the lower boundary as in DVM 1 with $r_{max} = 16\,400$ km. The simulation had twenty-seven points in r and twelve points in v, we call it DVM R. Figure 4.8 shows the outward molecular rates at steady state computed from DVM R. For DVM R the value at the former upper boundary is increased by 20% relative to DVM 1. The value of v_{esc} being smaller at higher altitude, the upper boundary condition would therefore let a greater part of the velocity distribution be in the escaping range.

4.3 Comparison to fluid-Jeans Model and DSMC

4.3.1 Comparing to fluid-Jeans model

We start by comparing the results of DVM 3 at steady state using the *fixed* condition to the results from the fluid-Jeans presented earlier. Figure 4.9 a shows that number density of DVM is consistent with the complete fluid-Jeans result. They both simulate a more appropriate number density than the barometric solution. Figure 4.9 b shows the temperature in DVM decreases more than the complete fluid-Jeans which becomes constant at high altitude. It becomes constant due to the assumed conduction at all altitude, which transfers energy through collisions and tends to homogenise temperature. Volkov et al. (2011) also shows that the Fourier law used for conduction in fluid-Jeans is an overestimate of the real conduction law and thus gives an overestimate of the temperature. Figure 4.9 c, shows that both the fluid-Jeans and the isothermal solutions have a small positive bulk velocity at the lower boundary as we expect from an escaping armosphere. Again, DVM has $u = 0$ at the lower boundary as a consequence of the choice of the lower boundary. In Figure 4.9 d, the reason for the zero escape rate of the lower boundary for DVM is the same

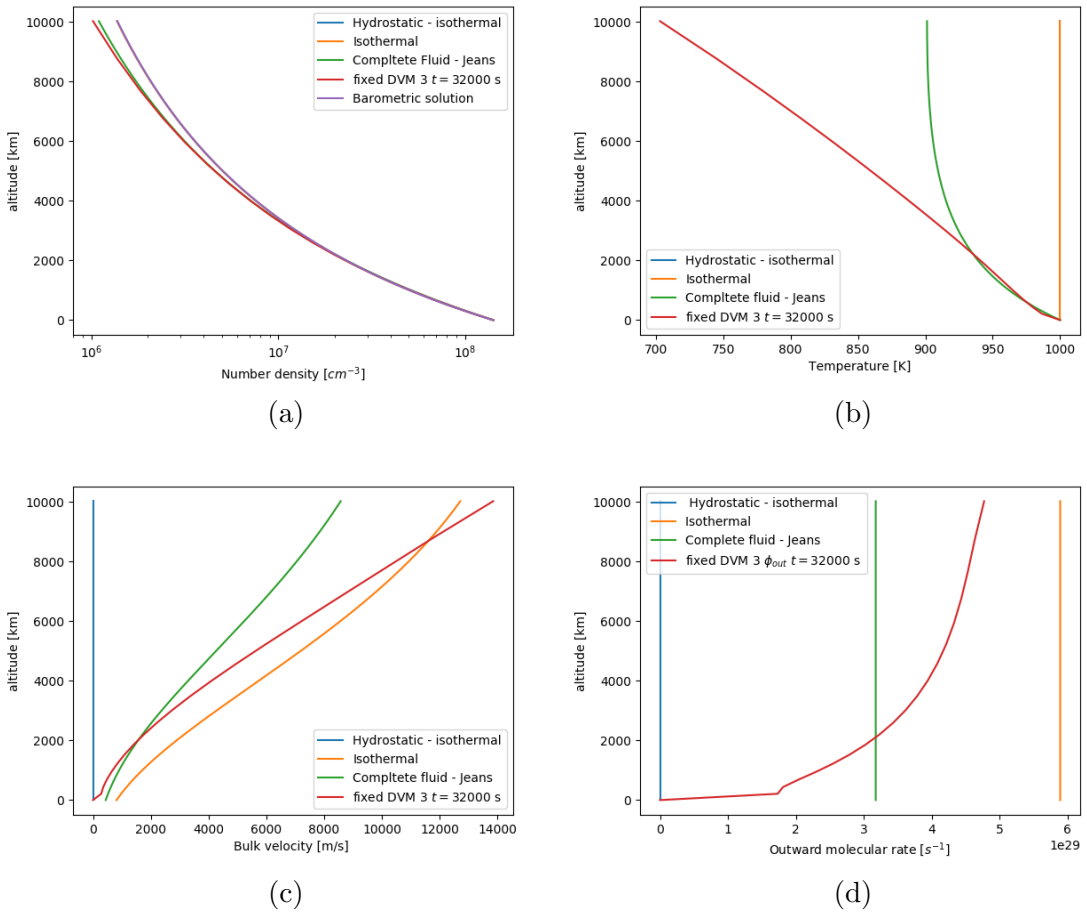

Figure 4.9: Profiles of macroscopic variables vs altitude. DVM 3 simulations with the *fixed* condition and fluid-Jeans simulation.

as for bulk velocity. At high altitude, the outward rate of DVM is larger than the complete fluid-Jeans rate. This is consistent with the enhanced escape with respect to Jeans escape at low λ (Volkov et al., 2011). Indeed, Jeans model is a correct approximation for slow escape process that happen at higher values of λ as shown in (Volkov et al., 2011).

4.3.2 Comparing to DSMC model

Let us now compare our results to those computed by Dr. Orenthal J. Tucker using a model of DSMC with the same parameters as we used.
Figure 4.10 a, shows number densities perfectly matching to each other. In Figure 4.10 b we see that the temperatures are relatively in good agreement. The DSMC result shows a temperature at lower boundary that has decreased with respet to T_0, while DVM is still close to T_0. In Figure 4.10 c, we see that DSMC has small issues at the boundaries. However, the bulk velocity trends are consistent and the values close to each others. Figure 4.10 d shows that DSMC has reach steady state and therefore, the value of its outward molecular rate is constant as expected for conservation of mass. The value computed for DVM is approaching the value of DSMC, while we can recall that the *specular* condition value could not reach steady

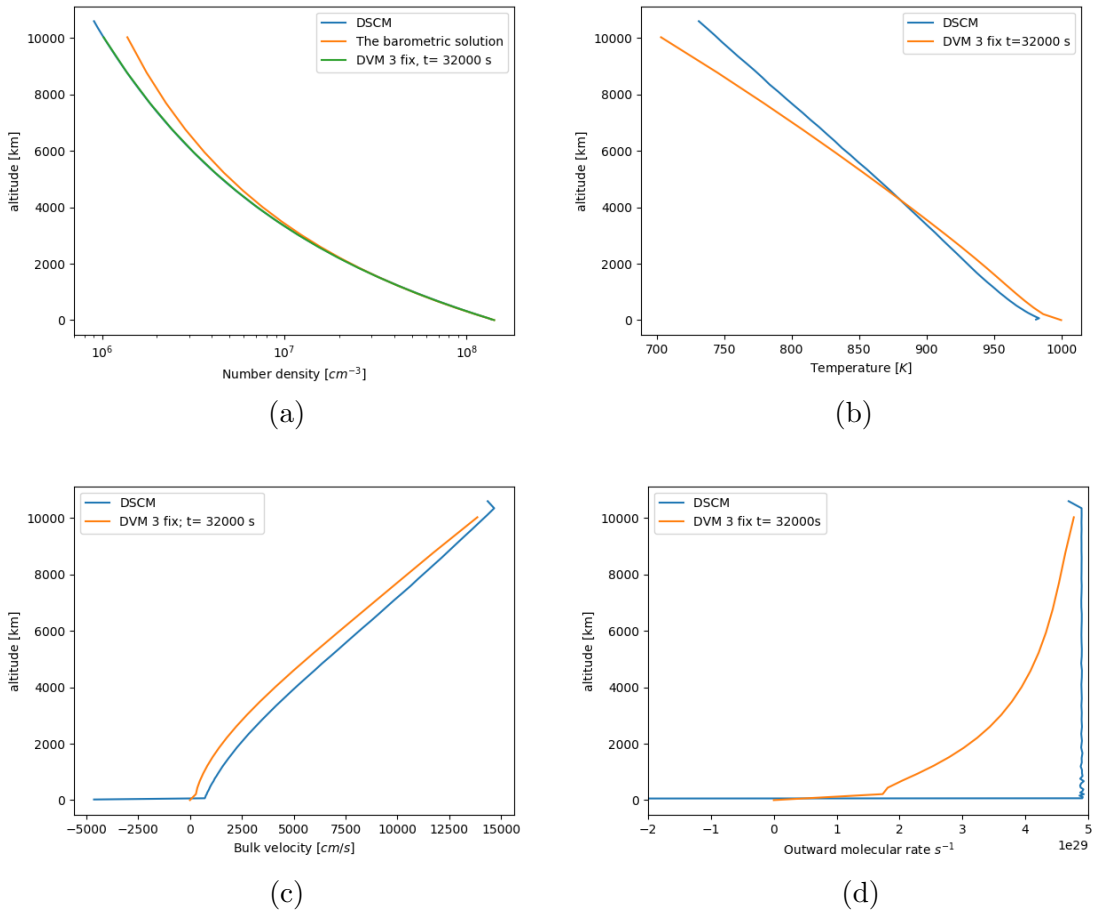

Figure 4.10: Profiles of macroscopic variables vs altitude. DVM simulations with the *fixed* condition and DSMC simulation. In Figure d, the x axes was croppped at -2×10^{29} s^{-1} .

state. This supports our choice for the use of *fixed* condition. DSMC boundary issues are still visible here. There is noise present in the lower altitudes and extremes values at the lower boundary. Finally, we look at the velocity distribution functions of both methods. We compute the one-dimensional distribution as a function of v_z as the DSMC data were only available in this form. In Figure 4.11 we clearly see that the velocity distribution at different altitudes are in good agreement for the two methods. The noise in DSMC is more apparent, particularly at sextreme value of velocity. However, we also see the DVM oscillations that were already discussed earlier. Even if the different noises are not in similar regions, the trends for both methods are consistent. Finally, both models show similar escaping and depleted tails, which would mean that they predict similar escape profiles.

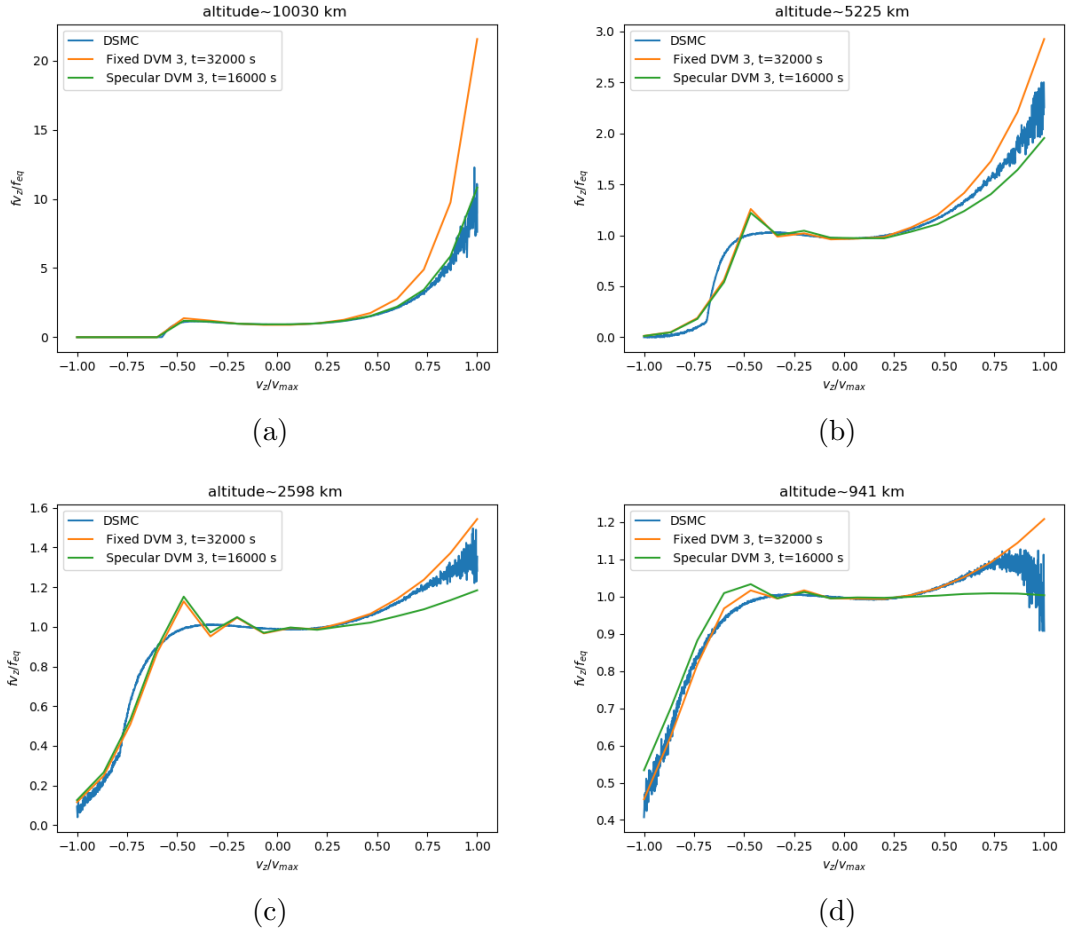

Figure 4.11: One dimensional velocity distribution function as a function of v_z for DVM 3 *fixed* condition after $t = 32\,000$ s; DVM 3 *specular* condition after $t = 16\,000$ s and DSMC at different altitudes. The function is scaled using the scaling distribution. Velocities are scaled to the maximum velocity of the domain which is 12 km . s^{-1}.

4.4 DVM on Pluto's Atmosphere

We have applied the DVM model to Pluto's amtopshere and we show the results here. We just had to replace the parameters and tune the grid to reach a stable solution. We chose to use a mass of 1.314×10^{25} g for the host body, a radius of $1\,450 \times 10^5$ cm for the radius of the host body, an atmosphere composed of nitrogen molecules, a lower boundary number density of $4.0 \times 10^{12}\text{cm}^{-3}$ and an initial temperature of 88.2 K. These values are similar to the values used by Erwin et al. (2012).
Furthermore, as seen in the DVM 1 model for Earth we had to resolve the Maxwellian distribution. Therefore, we had to encompass the escape velocity at upper boundary, which was equal to $v_{esc}(r_{max}) = 0.55$ km . s^{-1}, we thus chose a value of $v_{max} = 0.8$ km . s^{-1}. This allowed us to have velocity grid spacing of $\Delta v = 0.14545$ km . s^{-1} while the thermal velocity was $v_t = 0.22882$ km . s^{-1}. We also chose an upper boundary altitude of 5 800 km such that the lower boundary radial spacing was smaller than the scale height.
In Figure 4.12 we present the radial profiles of the macroscopic variables computed using the DVM 1 for Pluto's atmosphere. Even if a decrease in temperature and a non zero value can be seen for the bulk velocity, the model has no reach steady state. We actually see that the lower parts of the atmosphere, have not yet been altered by escape. We think that this is due to the value of the initial number density, which is four orders of magnitude larger than the one used for simulations on Earth. Indeed, the effects of the particles that have escaped have not had the time to influence the dense lower regions. This can be seen in Figure 4.13 c. We plotted the temperature radial profile at different times and we see that the lower regions have not been affected even after 32 000 sec. In Figure 4.13 a and b, we plotted one-dimensional velocity distributions at two different altitudes, we can see that in the lower parts the distribution has not departed from a Maxwellian because the effects of escape have not reached these altitudes.
In ongoing work, we will work on a longer time of simulations, or choose a higher lower boundary altitude in order to start with a less dense amtosphere. We will also investigate on combining the fluid model with DVM, choosing the later as an upper boundary to the former. We will base our work on a similar model that was developed for DSMC by Tucker et al. (2012) and Erwin et al. (2012).

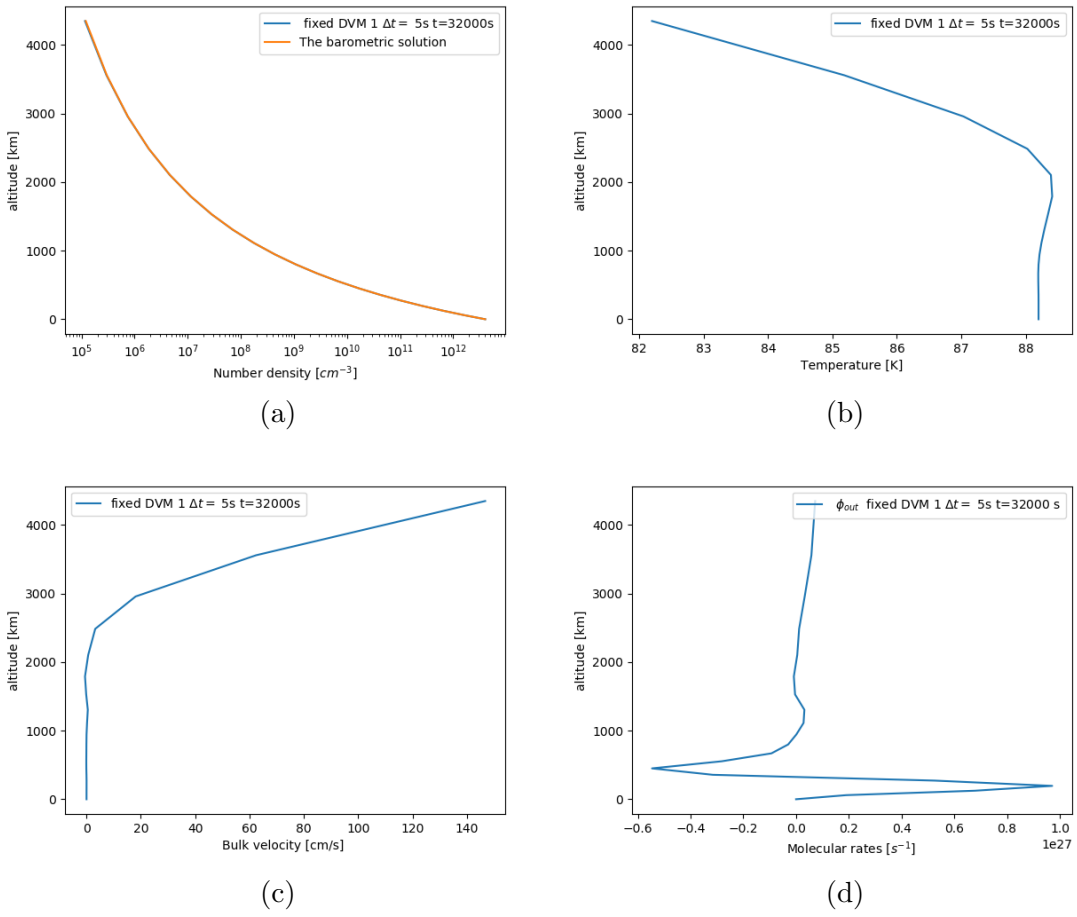

Figure 4.12: Profiles of macroscopic variables vs altitude. DVM 1 simulations with the *fixed* condition for Pluto's atmosphere.

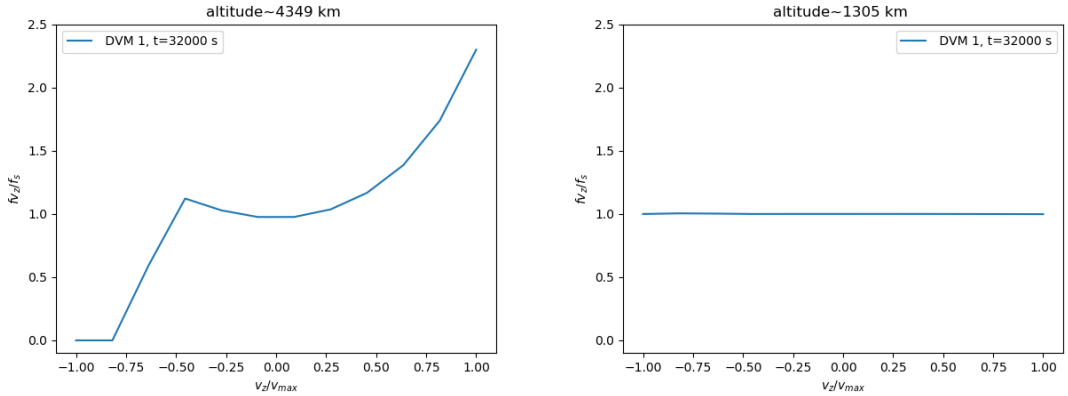

(a)

(b)

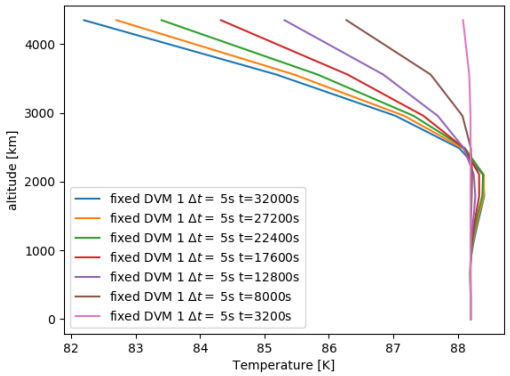

(c)

Figure 4.13: Temperature profile for different times and one-dimensional velocity distributions at two different altitudes. DVM 1 simulations with the *fixed* condition for Pluto's atmosphere.

Chapter 5

Conclusion

The purpose of this master's thesis was to work on atmospheric escape by revisiting an uncommonly used method in this context called the discrete velocity method rather than the usual direct simulation Monte-Carlo method. To do so, we reproduced the model presented in (Merryfield and Shizgal, 1994) who, to our knowledge, are the first to have applied discrete velocity to the problem of atmospheric escape. It is understandable that in the 90's when it took Merryfield and Shizgal (1994) an average of one month of computation time to obtain results, that the technique was somehow left aside for DSMC. However, even though this method is complex to implement, it is a straightforward and strong technique that has shown to be efficient as can be seen in the results presented here.

Indeed, even with the basic assumptions that we have done, we were able to produce results comparable in quality to fluid-Jeans and DSMC results. In addition, we have shown that the basic use of the method gives an insight into the properties of an atmosphere, while being more than three times as fast as usual DSMC simulations. We have also introduced a new lower boundary condition that works comparably to the one used in (Merryfield and Shizgal, 1994), but which, in our opinion, simulates a more realistic atmosphere. The DVM model does not present the statistical noise asssociated to DSMC, although still suffers from issues such as extreme values that do not seem to get smoothed out by a finer discretisation. as mentioned in the work. One could potentially consider virtual viscosity or other numerical techniques to reduce the peaks in the solutions. Furthermore, we could improved the realism of the model even more by using a drifting Maxwellian velocity distribution as a lower boundary. The model we have developed is, however, a basic model which considers an ideal atmosphere. It could be further improved in order to achieve better accuracy, i.e. by considering more complex atmospheres. The central equation, namely Boltzmann partial differential equation coupled to a non-linear collision integral, are still valid, but with some modifications. For example, using variable hard sphere or soft sphere particles would change the collision cross section term; considering ions and electrons would require to consider more interactions between particles through the acceleration term; considering multiple components would change the collision integral term.

It is easy to imagine the big, though interesting, challenge lying ahead and the very promising future of discrete velocity method regarding atmospheric escape problems.

Investigations should also be carried more deeply on the numerical methods used for the problem to improve the stability, robustness and efficiency of the method. Indeed, this method relies on solving a four-dimensional partial differential equation. This makes it very sensitive to the fineness of the discretization of the different dimensions, through the stability of the solutions and the computation time. Finally, we have solved the problem as Merryfield and Shizgal (1994) had written it, but there are probably other ways to circle the question and that might be more efficient.

Appendix A

Factorisation of the Velocity Distribution Function

As an initial condition for the velocity distribution of particles we chose to refer to (Merryfield and Shizgal, 1994). We thus have a distribution written as such

$$f_{eq}(r, v_x, v_y, v_z) = n(r) f_{mb}(v_x, v_y, v_z) \tag{A.1}$$

where $n(r)$ is the barometric number density, and f_{mb} the Maxwell-Boltzmann distribution. They are respectively given by

$$n(r) = n_0 \exp\left[\frac{r}{H(r)} - \frac{R}{H(R)}\right] \tag{A.2}$$

and

$$f_{mb} = \left(\frac{m}{2\pi k_b T}\right)^{\frac{3}{2}} \exp\left(-\frac{m(v_x^2 + v_y^2 + v_z^2)}{2k_b T}\right) \tag{A.3}$$

where n_0 is the number density at the surface of the planet, R is the radius of the planet and H is the scale height and is given by

$$H(r) = \frac{k_b T r^2}{GMm} \tag{A.4}$$

where G is the gravitational constant, M the mass of the chosen planet, m the mass of a particle, k_b the Boltzmann constant, T the temperature and r the radius where we consider the collision.
Now we introduce a prefactor, f_p, that takes the value by which our function is multiplied after an iteration. The distribution then becomes

$$f(r, v_x, v_y, v_z, t) = f_p(r, v_x, v_y, v_z, t) f_{eq}(r, v_x, v_y, v_z) \tag{A.5}$$

Now we can introduce this distribution in the form of the Boltzmann equation introduced in Equation 3.2

$$\frac{\partial f}{\partial t} + v_z \frac{\partial f}{\partial r} - \frac{1}{r}\left[v_x v_z \frac{\partial f}{\partial v_x} + v_y v_z \frac{\partial f}{\partial v_y} - (v_x^2 + v_y^2)\frac{\partial f}{\partial v_z}\right] - \frac{GM}{r^2}\frac{\partial f}{\partial v_z} = C[f] \tag{A.6}$$

As a consequence of the use of the prefactor, the derivatives are transformed as follows

$$\begin{aligned}\frac{\partial f}{\partial t} &= \frac{\partial f_{eq}.f_p}{\partial t} \\ &= \frac{\partial f_{eq}}{\partial t} f_p + f_{eq}\frac{\partial f_p}{\partial t} \\ &= 0 + f_{eq}\frac{\partial f_p}{\partial t}\end{aligned} \tag{A.7}$$

where the second term is evaluated numerically in the simulations. The spatial derivative is transformed as

$$\begin{aligned}\frac{\partial f}{\partial r} &= \frac{\partial f_{eq}.f_p}{\partial r} \\ &= \frac{\partial f_{eq}}{\partial r} f_p + f_{eq}\frac{\partial f_p}{\partial r} \\ &= \left(\frac{\partial n(r)}{\partial r} f_{mb} + n(r)\frac{\partial f_{mb}}{\partial r}\right) f_p + f_{eq}\frac{\partial f_p}{\partial r} \\ &= \left(-\frac{GMm}{k_b r^2 T} f_{eq} + 0\right) f_p + f_{eq}\frac{\partial f_p}{\partial r}\end{aligned} \tag{A.8}$$

where the second term is evaluated numerically in the simulations. The derivative with respect to v_x is transformed as

$$\begin{aligned}\frac{\partial f}{\partial v_x} &= \frac{\partial f_{eq}.f_p}{\partial v_x} \\ &= \frac{\partial f_{eq}}{\partial v_x} f_p + f_{eq}\frac{\partial f_p}{\partial v_x} \\ &= \left(\frac{\partial n(r)}{\partial v_x} f_{mb} + n(r)\frac{\partial f_{mb}}{\partial v_x}\right) f_p + f_{eq}\frac{\partial f_p}{\partial v_x} \\ &= \left(0 - \frac{m v_x}{k_b T} f_{eq}\right) f_p + f_{eq}\frac{\partial f_p}{\partial v_x}\end{aligned} \tag{A.9}$$

where the second term is evaluated numerically in the simulations. The derivative with respect to v_y is transformed as

$$\begin{aligned}\frac{\partial f}{\partial v_y} &= \frac{\partial f_{eq}.f_p}{\partial v_y} \\ &= \frac{\partial f_{eq}}{\partial v_y} f_p + f_{eq}\frac{\partial f_p}{\partial v_y} \\ &= \left(\frac{\partial n(r)}{\partial v_y} f_{mb} + n(r)\frac{\partial f_{mb}}{\partial v_y}\right) f_p + f_{eq}\frac{\partial f_p}{\partial v_y} \\ &= \left(0 - \frac{m v_y}{k_b T} f_{eq}\right) f_p + f_{eq}\frac{\partial f_p}{\partial v_y}\end{aligned} \tag{A.10}$$

where the second term is evaluated numerically in the simulations. The derivative with trspect to v_z is transformed as

$$\begin{aligned}\frac{\partial f}{\partial v_z} &= \frac{\partial f_{eq} f_p}{\partial v_z} \\ &= \frac{\partial f_{eq}}{\partial v_z} f_p + f_{eq} \frac{\partial f_p}{\partial v_z} \\ &= \left(\frac{\partial n(r)}{\partial v_z} f_{mb} + n(r) \frac{\partial f_{mb}}{\partial v_z} \right) f_p + f_{eq} \frac{\partial f_p}{\partial v_z} \\ &= \left(0 - \frac{m v_z}{k_b T} f_{eq} \right) f_p + f_{eq} \frac{\partial f_p}{\partial v_z} \end{aligned} \tag{A.11}$$

where the second term is evaluated numerically in the simulations. Accordingly, Equation A.6 can be rewritten as an equation in f_p

$$\left[\frac{\partial f_p}{\partial t} + c_z \frac{\partial f_p}{\partial r} - \frac{1}{r} \left[v_x v_z \frac{\partial f_p}{\partial v_x} + v_y v_z \frac{\partial f_p}{\partial v_y} - (v_x^2 + v_y^2) \frac{\partial f_p}{\partial v_z} \right] - \frac{GM}{r^2} \frac{\partial f_p}{\partial v_z} \right] f_{eq}$$

$$\begin{aligned} = \Bigg[v_z \left(\frac{GMm}{k_b r^2 T} \right) + \frac{1}{r} \Bigg(v_x v_z \left(-\frac{m v_x}{k_b T} \right) + v_y v_z \left(-\frac{m v_y}{k_b T} \right) \\ - (v_x^2 + v_y^2) \left(-\frac{m v_z}{k_b T} \right) \Bigg) + \frac{GM}{r^2} \left(-\frac{m v_z}{k_b T} \right) \Bigg] f_p f_{eq} + C[f] \end{aligned}$$

$$\left[\frac{\partial f_p}{\partial t} + c_z \frac{\partial f_p}{\partial r} - \frac{1}{r} \left[v_x v_z \frac{\partial f_p}{\partial v_x} + v_y v_z \frac{\partial f_p}{\partial v_y} - (v_x^2 + v_y^2) \frac{\partial f_p}{\partial v_z} \right] - \frac{GM}{r^2} \frac{\partial f_p}{\partial v_z} \right] = \frac{C[f]}{f_{eq}} \tag{A.12}$$

Appendix B

Non-Linear Boltzmann Equation

B.1 Right-Hand Side of the Non-Linear Boltzmann Equation

Following personal discussions and notes from Dr. Justin Erwin and refering to (Schunk and Nagy, 2000) here we detail how to discretise the continuous collision integral

$$\int\int [f_i' f_j' - f_i f_j] \sigma_{ij}(g_{ij}, \Omega) g_{ij} d\Omega dv_j^3 \tag{B.1}$$

as

$$\sum_{j=1}^{p} \sum_{k,l} A_{ij}^{kl} (f_k f_l - f_i f_j) \cdot \Delta v^3 \tag{B.2}$$

which may also be written as

$$\sum_{j=1}^{p} \sum_{k,l} \sigma_{ij}^{kl} |v_i - v_j| (f_k f_l - f_i f_j) \cdot \Delta v^3 \tag{B.3}$$

First, the integral over the velocity space is replaced by the sum over j, leading to

$$\int dv_j^3 \Rightarrow \sum_{j=1}^{p} \Delta v^3 \tag{B.4}$$

Then, the relative velocities are also identical and it is a matter of notations

$$g_{ij} \Rightarrow |v_i - v_j| \tag{B.5}$$

Furthermore, concerning the distributions f, they are also replaced and the $'$ are replaced by l and k. They represent the production terms of an (i, j) pair of particles, whereas $f_i f_j$ with a minus sign incarnate the loss of a pair of particles possessing velocity vectors v_i and v_j. Please refer to Section 2.4 for thorough explanations about the derivation of the collision integral.
We are left with the last remaining term which is not a straightforward replacement. Indeed, from (Schunk and Nagy, 2000, Chapter 4), we have

$$Q_T(g_{ij}) = \int \sigma_{ij}(g_{ij}, \Omega) d\Omega \tag{B.6}$$

which represents the total scattering cross section and is equal to πd^2 for a hard sphere particle, where d denotes the collisional diameter. Moreover, we consider that the outcomes of the collisions are all equally probable and that they only lie on a continuous sphere of diameter equal to g the relative velocity between the two particles and centered on the center of momentum of the colliding particles. The integration over Ω actually covers all the angles between pre- and post-collision velocity vectors and thus covers the whole sphere. So we can normalise the cross section with the surface of this sphere and we obtain the differential cross section,

$$\sigma_{ij}(g_{ij}, \Omega) = \frac{\pi d^2}{\pi g_{ij}^2} \tag{B.7}$$

If we take the discretised form, we consider that every outcome will lie on a single point of the sphere. These single points are the result of the intersection between the continuous sphere and the discretised three-dimensionnal velocity space. Therefore these outcomes do not cover the entire surface. However, we can normalise the cross section by summing over the number of post collision pairs of particles that lie on the sphere and we obtain the discrete differential cross section from

$$Q_T(g_{ij}) = \sum_{k,l} \sigma_{ij}^{kl} \tag{B.8}$$

which leads to

$$\sigma_{ij}^{kl} = \frac{\pi d^2}{C_{ij}} \tag{B.9}$$

with C_{ij} the total number of outcomes from the collision between particles with velocity vector i and j that lie on the previously defined sphere. Thus, the full form is as follows

$$\sum_{j=1}^{p} \sum_{k,l} \frac{\pi d^2}{C_{ij}} |v_i - v_j| (f_k f_l - f_i f_j) \cdot \Delta v^3 \tag{B.10}$$

B.2 Left-Hand Side of the Non-Linear Boltzmann Equation

Following personal discussions and notes from Dr. Guy Munhoven, here we detail how to express the general expression

$$\frac{\partial f}{\partial t} + (\vec{v} \cdot \nabla_r) f + (\vec{a} \cdot \nabla_v) f \tag{B.11}$$

in a coordinate system using spherical coordinates for the spatial components and a local Cartesian system for the velocity components, assuming azimuthal symmetry for the velocity components in this Cartesian system.

$$\frac{\partial f}{\partial t} + v_z \frac{\partial f}{\partial r} - \frac{1}{r} \left[v_x v_z \frac{\partial f}{\partial v_x} + v_y v_z \frac{\partial f}{\partial v_y} - (v_x^2 + v_y^2) \frac{\partial f}{\partial v_z} \right] - \frac{GM}{r^2} \frac{\partial f}{\partial v_z} \tag{B.12}$$

First, we start by setting the azimuthal symmetry of a function f with respect to $\vec{v}$. This symetry involves

$$\frac{\partial f}{\partial \phi} = 0 \tag{B.13}$$

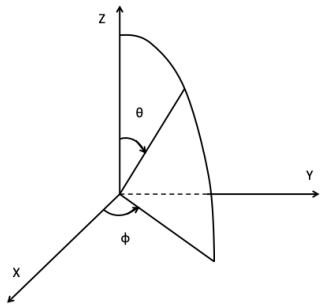

Figure B.1: Cartesian coordinates system.

Furthermore, a general vector $\vec{v}$ can be written with Cartesian coordinates as

$$\vec{v} = v_x\vec{e_x} + v_y\vec{e_y} + v_z\vec{e_z} \tag{B.14}$$

with its components being the projection of v, the norm of the vector, on the axes in Figure B.1 such as

$$v_x = v\ \cos\phi \sin\theta \tag{B.15}$$
$$v_y = v\ \sin\phi \sin\theta \tag{B.16}$$
$$v_z = c\ \cos\theta \tag{B.17}$$

The term in the left-hand side of Equation B.13 can be written in an other way

$$\begin{aligned}\frac{\partial f}{\partial \phi} &= \frac{\partial f}{\partial v_x}\frac{\partial v_x}{\partial \phi} + \frac{\partial f}{\partial v_y}\frac{\partial v_y}{\partial \phi} + \frac{\partial f}{\partial v_z}\frac{\partial v_z}{\partial \phi} \\ &= \frac{\partial f}{\partial v_x} v(-\sin\phi)\sin\theta + \frac{\partial f}{\partial v_y} v\ \cos\phi\ \sin\theta + \frac{\partial f}{\partial v_z}\cdot 0 \\ &= \frac{\partial f}{\partial v_x}(-v_y) + \frac{\partial f}{\partial v_y} v_x \end{aligned} \tag{B.18}$$

Azimuthal symmetry thus translates to

$$\frac{\partial f}{\partial \phi} = 0 \Leftrightarrow \frac{\partial f}{\partial v_x} v_y = \frac{\partial f}{\partial v_y} v_x \tag{B.19}$$

Now, the time derivative in Equation B.11 stays unchanged and the last term can be developed and we get

$$\vec{a}(r) = -\frac{GM}{r^2}\vec{\rho} \tag{B.20}$$
$$\nabla_v f = \frac{\partial f}{\partial v_x}\vec{\phi} - \frac{\partial f}{\partial v_y}\vec{\theta} + \frac{\partial f}{\partial v_z}\vec{\rho} \tag{B.21}$$

Since $\vec{\rho} \perp \vec{\phi}$; $\vec{\theta} \perp \vec{\rho}$, we obtain

$$\begin{aligned}\vec{a}(r)\cdot\nabla_v f &= -\frac{GM}{r^2}\vec{\rho}\cdot\frac{\partial f}{\partial v_z}\vec{\rho} \\ &= -\frac{GM}{r^2}\cdot\frac{\partial f}{\partial v_z}\end{aligned} \tag{B.22}$$

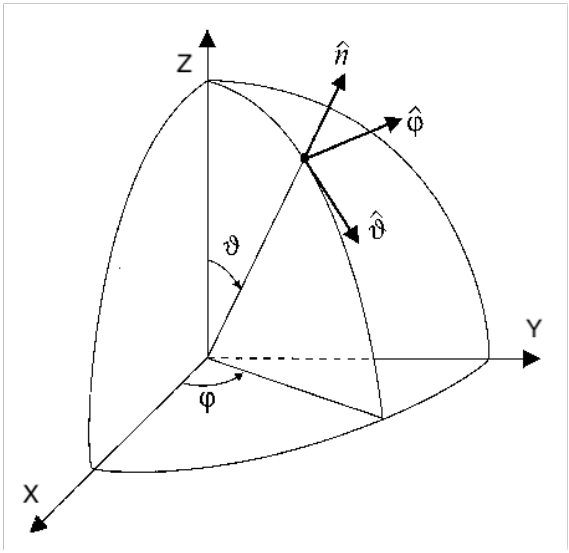

Figure B.2: Spherical coordinates system from (Mishchenko and Travis, 2003)

To derive the remaining term, we need to introduce the system of coordinate from Figure B.2, which is a coordinate system showing a fixed Cartesian system of axes represented by $(\vec{X}, \vec{Y}, \vec{Z})$ coupled to a mobile Cartesian system of axes represented by $(\vec{\rho}, \vec{\theta}, \vec{\phi})$ and linked to the transformation of the fixed Cartesian coordinate system to a fixed spherical coordinate system. In this Figure, the vector v is the one pointing in the direction of the vector n. In the mobile system, the x coordinate is taken positive eastwards (following $\vec{\phi}$), the y coordinate is taken positive northwars (following $-\vec{\theta}$) and the z coordinate is taken positive away from the center (following $\vec{\rho}$). The former can be expressed as follows in the mobile system

$$\vec{v} = v_x \cdot \vec{\phi} - v_y \cdot \vec{\theta} + \vec{v_z} \cdot \vec{\rho} \tag{B.23}$$

and as follows in the fixed system

$$\vec{v} = V_X \vec{e_X} + V_Y \vec{e_Y} + V_Z \vec{e_Z} \tag{B.24}$$

Furthermore, we project the unit vectors of the system on the other axes, which gives us:

$$\vec{e_X} = \sin\theta \ \cos\phi \ \vec{\rho} + \cos\theta \ \cos\phi \ \vec{\theta} - \sin\phi \ \vec{\phi} \tag{B.25}$$

$$\vec{e_Y} = \sin\theta \ \sin\phi \ \vec{\rho} + \cos\theta \ \sin\phi \ \vec{\theta} + \cos\phi \ \vec{\phi} \tag{B.26}$$

$$\vec{e_Z} = \cos\theta \ \vec{\rho} - \sin\theta \ \vec{\theta} \tag{B.27}$$

Then, we introduce Eqns. B.25–B.27 into Equation B.24 and group the terms according to the unit vectors to obtain

$$\begin{aligned} \vec{v} =& (V_X \ \sin\theta \ \cos\phi + V_Y \ \sin\phi \ \sin\theta + V_Z \ \cos\theta)\vec{\rho} \\ &+ (V_X \ \cos\theta \ \cos\phi + V_Y \ \sin\phi \ \cos\theta - V_Z \ \sin\theta)\vec{\theta} \\ &+ (-V_X \sin\phi + V_Y \ \cos\phi)\vec{\phi} \end{aligned} \tag{B.28}$$

We apply the same manipulations to the other unit vectors

$$\vec{\rho} = \sin\theta\ \cos\phi\ \vec{e_X} + \sin\theta\ \sin\phi\ \vec{e_Y} + \cos\theta\ \vec{e_Z} \tag{B.29}$$

$$\vec{\theta} = \cos\theta\ \cos\phi\ \vec{e_X} + \cos\theta\ \sin\phi\ \vec{e_Y} - \sin\theta\ \vec{e_Z} \tag{B.30}$$

$$\vec{\phi} = -\sin\phi\ \vec{e_X} + \cos\phi\ \vec{e_Y} \tag{B.31}$$

and derive

$$\begin{aligned}\vec{v} =&(v_x\ (-\sin\phi) - v_y\ \cos\phi\ \cos\theta + v_z\ \sin\theta\ \cos\phi)\vec{e_X}\\ &+ (v_x\ \cos\phi - v_y\ \sin\phi\ \cos\theta + v_z\ \sin\theta\ \sin\phi)\vec{e_Y}\\ &+ (v_y\ \sin\theta + v_z\ \cos\theta))\vec{e_Z}\end{aligned} \tag{B.32}$$

Therefore, we can define the components from each system as follows, using Equations B.24 and B.32

$$V_X = v_x\ (-\sin\phi) - v_y\ \cos\phi\ \cos\theta + v_z\ \sin\theta\ \cos\phi \tag{B.33}$$

$$V_Y = v_x\ \cos\phi - v_y\ \sin\phi\ \cos\theta + v_z\ \sin\theta\ \sin\phi \tag{B.34}$$

$$V_Z = v_y\ \sin\theta + v_z\ \cos\theta \tag{B.35}$$

and using Equations B.23 and B.28

$$v_x = -V_X \sin\phi + V_Y\ \cos\phi \tag{B.36}$$

$$v_y = -V_X\ \cos\theta\ \cos\phi - V_Y\ \sin\phi\ \cos\theta + V_Z\ \sin\theta \tag{B.37}$$

$$v_z = V_X\ \sin\theta\ \cos\phi + V_Y\ \sin\phi\ \sin\theta + V_Z\ \cos\theta \tag{B.38}$$

As they will be needed, we derive the derivatives with respect to ϕ and θ of Equations B.36, B.37 and B.38

$$\begin{aligned}\frac{\partial v_x}{\partial\phi} =& -V_X\cos\phi - V_Y\ \sin\phi\\ =&(v_y - V_Z\sin\theta)/\cos\theta\\ =&(v_y - v_y\sin^2\theta - V_Z\sin\theta\cos\theta)/\cos\theta\\ =&(v_y\cos^2\theta - V_Z\sin\theta\cos\theta)/\cos\theta\\ =&v_y\cos\theta - v_z\sin\theta\end{aligned} \tag{B.39}$$

$$\frac{\partial v_y}{\partial\phi} = V_X\ \cos\theta\ \sin\phi - V_Y\ \cos\phi\ \cos\theta = -\cos\theta v_x \tag{B.40}$$

$$\frac{\partial v_z}{\partial\phi} = -V_X\ \sin\theta\ \sin\phi + V_Y\ \cos\phi\ \sin\theta + V_Z\ \cos\theta = \sin\theta v_x \tag{B.41}$$

$$\frac{\partial v_x}{\partial\theta} = 0 \tag{B.42}$$

$$\frac{\partial v_y}{\partial\theta} = V_X\ \sin\theta\ \cos\phi + V_Y\ \sin\phi\ \sin\theta + V_Z\cos\theta = v_z \tag{B.43}$$

$$\frac{\partial v_z}{\partial\theta} = V_X\ \cos\theta\ \cos\phi + V_Y\ \sin\phi\ \cos\theta - V_Z\ \sin\theta = -v_y \tag{B.44}$$

We can derive the second term of Equation B.11, i.e. the gradient is given in spherical coordinates as

$$\nabla_r f = \frac{\partial f}{\partial r}\vec{\rho} + \frac{1}{r\ \sin\theta}\frac{\partial f}{\partial\phi}\vec{\phi} + \frac{1}{r}\frac{\partial f}{\partial\theta}\vec{\theta} \tag{B.45}$$

Combining with the definition B.23 we have

$$\begin{aligned}
\vec{v}\cdot\nabla_r f &= (v_x\cdot\vec{\phi} - v_y\cdot\vec{\theta} + \vec{v_z}\cdot\vec{\rho})\left(\frac{\partial f}{\partial r}\vec{\rho} + \frac{1}{r\ \sin\theta}\frac{\partial f}{\partial\phi}\vec{\phi} + \frac{1}{r}\frac{\partial f}{\partial\theta}\vec{\theta}\right)\\
&= v_x\frac{1}{r\ \sin\theta}\frac{\partial f}{\partial\phi} - v_y\frac{1}{r}\frac{\partial f}{\partial\theta} + v_z\frac{\partial f}{\partial r}\\
&= v_z\frac{\partial f}{\partial r} + v_x\frac{1}{r\ \sin\theta}\left[\frac{\partial f}{\partial v_x}\frac{\partial v_x}{\partial\phi} + \frac{\partial f}{\partial v_y}\frac{\partial v_y}{\partial\phi} + \frac{\partial f}{\partial v_z}\frac{\partial v_z}{\partial\phi}\right]\\
&\qquad - v_y\frac{1}{r}\left[\frac{\partial f}{\partial v_x}\frac{\partial v_x}{\partial\theta} + \frac{\partial f}{\partial v_y}\frac{\partial v_y}{\partial\theta} + \frac{\partial f}{\partial v_z}\frac{\partial v_z}{\partial\theta}\right]\\
&= v_z\frac{\partial f}{\partial r} + v_x\frac{1}{r\ \sin\theta}\left[\frac{\partial f}{\partial v_x}(v_y\cos\theta - v_z\sin\theta)\right.\\
&\qquad\qquad + \frac{\partial f}{\partial v_y}(-\cos\theta v_x)\\
&\qquad\qquad \left. + \frac{\partial f}{\partial v_z}\sin\theta v_x\right]\\
&\qquad - v_y\frac{1}{r}\left[\frac{\partial f}{\partial v_x}\cdot 0 + \frac{\partial f}{\partial v_y}v_z - \frac{\partial f}{\partial v_z}v_y\right]
\end{aligned}$$

where we used the fact that the function f depends on θ and ϕ only through v_x, v_y and v_z and where we used Equations B.39 - B.44

$$\begin{aligned}
&= v_z\frac{\partial f}{\partial r} + v_x\frac{1}{r\ \sin\theta}\left[\underbrace{\left(\frac{\partial f}{\partial v_x}v_y - \frac{\partial f}{\partial v_y}v_x\right)}_{=0.\ \textit{Azimuthal symmetry}}\cos\theta - v_z\sin\theta\frac{\partial f}{\partial v_x} + \frac{\partial f}{\partial v_z}\sin\theta\right]\\
&\qquad - v_y\frac{1}{r}\left[\frac{\partial f}{\partial v_y}v_z - \frac{\partial f}{\partial v_z}v_y\right]\\
&= v_z\frac{\partial f}{\partial r} + \frac{1}{r}\left[-v_xv_z\frac{\partial f}{\partial v_x} + v_x^2\frac{\partial f}{\partial v_z} - v_zv_y\frac{1}{r}\frac{\partial f}{\partial v_y} + v_y^2\frac{\partial f}{\partial v_z}\right]\\
&= v_z\frac{\partial f}{\partial r} - \frac{1}{r}\left[v_xv_z\frac{\partial f}{\partial v_x} + v_yv_z\frac{\partial f}{\partial v_y} - (v_x^2+v_y^2)\frac{\partial f}{\partial v_z}\right] \qquad \text{(B.46)}
\end{aligned}$$

Finally, we inject Equations B.22 and B.46 in Equation B.11 to retrieve Equation B.12

$$\frac{\partial f}{\partial t} + v_z\frac{\partial f}{\partial r} - \frac{1}{r}\left[v_xv_z\frac{\partial f}{\partial v_x} + v_yv_z\frac{\partial f}{\partial v_y} - (v_x^2+v_y^2)\frac{\partial f}{\partial v_z}\right] - \frac{GM}{r^2}\frac{\partial f}{\partial v_z} \qquad \text{(B.47)}$$

Appendix C

Jeans Escape Flux Formula

From integrating the statistical Maxwell-Boltzmann distribution over the velocity space we can derive the Jeans escape flux of particles given as

$$F_J = n\sqrt{\frac{k_b T}{2m\pi}}(1 + \frac{GMm}{k_b Tr})\exp(-\frac{GMm}{k_b Tr}) \tag{C.1}$$

The distribution is written as

$$f(\vec{v}) = \left(\frac{m}{2\pi T k_b}\right)^{\frac{3}{2}} \exp\left(\frac{m\vec{v}.\vec{v}}{2Tk_b}\right) \tag{C.2}$$

In order to get the flux we need to integrate over the velocity space and multiply by the number density and the z component of velocity as follows

$$F = \int n v_z f(\vec{v}) dv^3 \tag{C.3}$$

Now, using the spherical coordinates, the escape flux is derived as the integral of the number of particles with $v_z > 0$ and $v > v_{esc}$.

$$F_J = \int_0^{\frac{\pi}{2}} \int_0^{2\pi} \int_{v_{esc}}^{\infty} nv \cos\theta f(\vec{v}) v^2 \sin\theta \, dv \, d\phi \, d\theta \tag{C.4}$$

Since $v_z = v\cos\theta$ this requires that $0 < \theta < \frac{\pi}{2}$ and $v > v_{esc}$. Integrating over the angles allows to derive

$$\begin{aligned} F_J =& n \int_0^{\frac{\pi}{2}} \cos\theta \sin\theta d\theta \int_0^{2\pi} d\phi \int_{v_{esc}}^{\infty} f(\vec{v}) v^3 dv \\ =& n\pi \int_{v_{esc}}^{\infty} f(\vec{v}) v^3 dv \end{aligned} \tag{C.5}$$

We denote the thermal velocity $\sqrt{\frac{2k_b T}{m}}$ by v_t and introduce the change of variable

$$x = \frac{v}{v_t} \rightarrow dx = \frac{dv}{v_t}$$
$$dx \cdot v_t = dv$$

$$\text{Since } x \to \infty \text{ as } v \to \infty$$
$$\text{and } x \to \frac{v_{esc}}{v_t} \text{ as } v \to v_{esc}$$

Equation C.5 becomes

$$F_J = \left(\frac{m}{2\pi T k_b}\right)^{\frac{3}{2}} v_t^4 n\pi \int_{\frac{v_{esc}}{v_t}}^{\infty} \exp(-x^2)x^3 dx \tag{C.6}$$

The integral can be integrated by parts following

$$\int_a^b u(x)v'(x)dw = uv|_a^b - \int_a^b u'(x)v(x)dx \tag{C.7}$$

with

$$u(x) = x^2$$
$$v'(x) = \frac{-1}{2} - 2x\exp(-x^2)$$

Hence

$$\begin{aligned}
\int_{\frac{v_{esc}}{v_t}}^{\infty} \exp(-x^2)x^3 dx =& \frac{-1}{2}\left[x^2\exp(-x^2)\frac{-2x}{-2x}|_{\frac{v_{esc}}{v_t}}^{\infty} - \int_{\frac{v_{esc}}{v_t}}^{\infty} 2x\exp(-x^2)dx\right] \\
&\Leftrightarrow \frac{-1}{2}\left(0 - \frac{v_{esc}^2}{v_t^2}\exp\left(\frac{v_{esc}}{v_t}\right)^2\right) + \frac{-1}{2}\int_{\frac{v_{esc}}{v_t}}^{\infty} 2x\exp(-x^2)dx \\
&\Leftrightarrow \frac{1}{2}\frac{v_{esc}^2}{v_t^2}\exp\left(\frac{v_{esc}}{v_t}\right)^2 - \frac{1}{2}\exp(-x^2)|_{\frac{v_{esc}}{v_t}}^{\infty} \\
&\Leftrightarrow \frac{1}{2}\left(\frac{v_{esc}^2}{v_t^2}+1\right)\exp\left(\frac{v_{esc}}{v_t}\right)^2
\end{aligned} \tag{C.8}$$

Equation C.6 finally becomes

$$\begin{aligned}
F_J =& \left(\frac{m}{2\pi T k_b}\right)^{\frac{3}{2}} v_t^4 n\pi \frac{1}{2}\left(\frac{v_{esc}^2}{v_t^2}+1\right)\exp\left(\frac{v_{esc}}{v_t}\right)^2 \\
=& \left(\frac{m}{2\pi T k_b}\right)^{\frac{3}{2}} \left(\frac{2k_bT}{m}\right)^2 n\pi \frac{1}{2}\left(\frac{v_{esc}^2}{v_t^2}+1\right)\exp\left(\frac{v_{esc}}{v_t}\right)^2 \\
=& \sqrt{\frac{Tk_b}{2\pi m}} n\left(1+\frac{GMm}{rk_bT}\right)\exp\left(-\frac{GMm}{rk_bT}\right)
\end{aligned} \tag{C.9}$$

Bibliography

Arnst, M. (2018). Modeling with partial differential equations. `http://hdl.handle.net/2268/224880`.

Banks, P. and Kockarts, G. (1973). *Aeronomy*. Number ptie. 1 in Aeronomy. Academic Press.

Bird, G. (1994). *Molecular Gas Dynamics and the Direct Simulation of Gas Flows*. Number vol. 1 in Molecular Gas Dynamics and the Direct Simulation of Gas Flows. Clarendon Press.

Broadwell, J. E. (1964). Study of rarefied shear flow by the discrete velocity method. *Journal of Fluid Mechanics*, 19:401 – 414.

Cabannes, H. (1976). Couette flow for a gas with a discrete velocity distribution. *Journal of Fluid Mechanics*, 76(2):273–287.

Catling, D. C. and Kasting, J. F. (2017). *Escape of Atmospheres to Space*, pages 129–168. Cambridge University Press.

Chamberlain, J. W. (1963). Planetary coronae and atmospheric evaporation. *Planetary and Space Science*, 11(8):901 – 960.

Clette, F. (2017-2018). *Solar physics, activity phenomena and Sun-Earth relations*. Université de Liège.

Dimarco, G. and Pareschi, L. (2014). Numerical methods for kinetic equations. *Acta Numerica*, 23:369–520.

Erwin, J., Tucker, O., and E. Johnson, R. (2012). Hybrid fluid/kinetic modeling of pluto's escaping atmosphere. *Icarus*, 226.

Gatignol, R. (1975). Kinetic theory for a discrete velocity gas and application to the shock structure. *Physics of Fluids*, 18:153–161.

Grodent, D. (2018 - 2019). *Atmosphere of the Earth*. Université de Liège.

Hirsch, C. (2007). Numerical computation of internal and external flows,. In *Fundamentals of Computational Fluid Dynamics*, volume 1, chapter 7. Elsevier, 2 edition.

Inamuro, T. and Sturtevant, B. (1990). Numerical study of discrete-velocity gases. *Physics of Fluids A: Fluid Dynamics*, 2(12):2196–2203.

Isaacson, E. and B. Keller, H. (1994). Analysis of numerical methods. chapter 9. Dover Publications.

Jeans, J. H. (1916). *The Dynamical Theory of Gases*. Cambridge University Press, 4th edition.

Krasnopolsky, V. A. (2019). *Spectroscopy and Photochemistry of Planetary Atmospheres and Ionospheres: Mars, Venus, Titan, Triton and Pluto*. Cambridge Planetary Science. Cambridge University Press.

Merryfield, W. J. and Shizgal, B. D. (1994). Discrete velocity model for an escaping single-component atmosphere. *Planetary and Space Science - PLANET SPACE SCI*, 42:409–419.

Mishchenko, M. I. and Travis, L. D. (2003). Electromagnetic scattering by nonspherical particles. *Exploring the Atmosphere by Remote Sensing Techniques*.

Morton, K. W. and Mayers, D. F. (2005). Numerical solution of partial differential equations. chapter 4. Cambridge University Press, second edition.

Palharini, R. (2014). *Atmospheric Reentry Modelling Using an Open-Source DSMC Code*. PhD thesis.

Parker, E. (1964). Dynamical properties of stellar coronas and stellar winds. i. integration of the momentum equation. *Astrophysical Journal (U.S.)*, Vol: 139.

Pierrard, V. (2003). Evaporation of hydrogen and helium atoms from the atmospheres of earth and mars. *Planetary and Space Science*, 51(4):319 – 327.

Schunk, R. W. and Nagy, A. (2000). *Ionospheres: Physics, Plasma Physics, and Chemistry, Atmos. Space Sci. Ser.*

Shizgal, B. and Arkos, G. G. (1996). Nonthermal escape of the atmospheres of venus, earth, and mars. *Reviews of Geophysics - REV GEOPHYS*, 34.

Silber, E. (2018). Meteor science infrasound observations of bright meteors: the fundamentals. 46:52.

Tucker, O. J., Erwin, J. T., Deighan, J. I., Volkov, A. N., and Johnson, R. E. (2012). Thermally driven escape from Pluto's atmosphere: A combined fluid/kinetic model. *Icarus*, 217(1):408–415.

Tucker, O. J. and Johnson, R. (2009). Thermally driven atmospheric escape: Monte carlo simulations for titan's atmosphere. *Planetary and Space Science*, 57(14):1889 – 1894.

Volkov, A. N., Johnson, R. E., Tucker, O. J., and Erwin, J. T. (2011). Thermally driven atmospheric escape: transition from hydrodynamic to jeans escape. *The Astrophysical Journal*, 729(2):L24.